

A Physics-Regularized Neural Network and Kirchhoff Markov Random Field Framework for Inferring Internal Electrochemical States from Operando Spectromicroscopy

Naoki Wada^{1*}, Yuta Kimura², Masaichiro Mizumaki³, Koji Amezawa², Ichiro Akai⁴, Toru Aonishi^{1*}

1 Graduate School of Frontier Sciences, The University of Tokyo, Japan

2 Institute of Multidisciplinary Research for Advanced Materials, Tohoku University, Japan

3 Graduate School of Science and Technology, Kumamoto University, Japan

4 Institute of Industrial Nanomaterials, Kumamoto University, Japan

* These two authors contributed equally to this work

Corresponding Author: Toru Aonishi (aonishi@edu.k.u-tokyo.ac.jp)

Abstract

Quantitative understanding of coupled reaction and transport processes in lithium-ion battery (LIB) composite electrodes remains challenging because key internal states cannot be measured directly. In this study, we develop a physics-integrated, data-driven analysis pipeline to estimate internal electrochemical states from operando microscopic X-ray absorption fine structure (μ -XAFS) hyperspectral data of LIB cathodes with LiPF_6 electrolyte. State-of-charge (SOC) maps are first constructed from Co K-edge spectra. To resolve ambiguities in the two-phase reaction region, a physics-regularized three-layer neural network is introduced, enforcing spatial continuity of SOC and current conservation. The inferred SOC dynamics are then incorporated into a Kirchhoff-based Markov random field framework that integrates Kirchhoff's current and voltage laws, Ohm's law, and a symmetric Butler-Volmer relation to estimate interfacial current, ionic current, electrolyte potential, and effective ionic conductivity. Application to composite electrodes with different initial

electrolyte concentrations (0.3, 1, and 2 M LiPF₆) reveals distinct reaction propagation behaviors governed by electrolyte concentration-dependent conductivity. The inferred electrolyte concentration distributions show qualitative agreement with independent operando X-ray transmission imaging performed on LIB composite cathodes employing a LiAsF₆ electrolyte. This framework enables quantitative visualization of otherwise inaccessible internal transport phenomena.

Acknowledgments

This work is supported by JST CREST Grant No. JPMJCR1861, JPMJCR2431 and JPMJCR2432.

1. Introduction

In response to the increasing performance demands of portable electronic devices, electric micromobility systems, and drones, as well as the widespread adoption of electric vehicles and the large-scale integration of renewable energy sources, there is a strong demand for the development of lithium-ion rechargeable batteries (LIBs) with high energy density and high reliability [1–6]. To meet these requirements, it is essential to understand in detail the mechanisms of charge-discharge reactions occurring within LIB electrodes and to optimize electrode structures and material design based on the knowledge obtained.

The charge-discharge reactions in LIB composite electrodes are highly complex processes involving strongly coupled phenomena, including lithium-ion transport in the electrolyte, electron transport through conductive additives and active materials, charge transfer at the active material/electrolyte interface, and lithium diffusion within active material particles [7]. Moreover, owing to the complex microstructures formed by active materials, conductive additives, and binders, as well as the intricate ionic and electronic conduction pathways, these reactions proceed spatially inhomogeneously within the electrode. Their spatial distributions evolve dynamically as charging and discharging progress [8–11].

Against this background, attempts have been made to directly capture the overall behavior of charge-discharge reactions in composite electrodes using advanced

characterization techniques. For example, spatial inhomogeneity of lithium concentration (Li heterogeneity) in active materials has been evaluated using scanning / full-field synchrotron X-ray microspectroscopy [12–16]. In addition, spatially inhomogeneous electrolyte salt concentration distributions arising from local stagnation of lithium-ion transport in the electrolyte have been visualized using X-ray fluorescence analysis [17], magnetic resonance imaging [18,19], and phase-contrast X-ray imaging [20]. However, these techniques capture only one aspect of electrode reactions and have not led to a comprehensive understanding of the entire reaction process in which multiple transport and reaction processes are strongly coupled.

On the other hand, numerical simulations based on porous electrode models have been developed to reproduce charge-discharge reactions within electrodes and to infer the underlying mechanisms [21–27]. In particular, lithium-ion transport simulations using electrode pore structures obtained by X-ray CT [23], simulations incorporating the structure of the carbon binder domain phase obtained by X-ray CT [24,25], and the development of Python libraries for implementing such simulations [27] have been reported. While these numerical simulations are valuable, important parameters such as exchange current density are often not sufficiently determined experimentally and must be assumed. Moreover, the validity of simulation results has typically been assessed only indirectly through their consistency with macroscopic electrode responses, such as charge-discharge curves and capacity. Direct verification of the spatiotemporal dynamics of reactions occurring inside the electrode remains difficult.

In recent years, data-driven scientific approaches based on machine learning have been increasingly employed to extract latent structures embedded in hyperspectral images acquired by techniques such as scanning transmission electron microscopy-electron energy loss spectroscopy (STEM-EELS), Raman spectroscopy, and synchrotron microspectroscopy [28–34]. Applications include compound labeling and noise reduction using non-negative matrix factorization (NMF) [28–30,33,34], analysis of electronic state distributions by combining Bayesian spectroscopy [34–36] with NMF [31], and phase behavior analysis in conjunction with operando pair distribution function measurements [32]. Applying such methods to spatiotemporal measurement data of charge-discharge reactions may enable simultaneous extraction of insights into the material transport and charge-transfer processes governing the reactions.

In this study, we develop an analysis pipeline to reconstruct hidden electrochemical states in lithium-ion battery (LIB) composite cathodes from operando microscopic X-

ray absorption fine structure (μ -XAFS) hyperspectral data. By leveraging the spatiotemporal spectral evolution associated with charge-discharge reactions, the framework enables quantitative inference of internal transport variables that are not directly accessible from spectroscopy alone, including solid-liquid interfacial current and potential difference, liquid-phase ohmic resistance, and electrolyte concentration dynamics.

The pipeline consists of two components. First, a physics-regularized three-layer neural network (NN) estimates state-of-charge (SOC) distributions, including regions with minimal spectral sensitivity to lithium insertion/extraction. Spatial continuity of SOC and current conservation are imposed as constraints to ensure stable reconstruction. Second, the inferred SOC dynamics are incorporated into a Kirchhoff-Markov random field (MRF) framework based on a simplified porous electrode equivalent circuit. By integrating Kirchhoff's laws, Ohm's law, and interfacial reaction kinetics within a probabilistic formulation, the model consistently estimates internal transport-related state variables.

The method is applied to operando datasets obtained from composite electrodes with three different initial LiPF_6 electrolyte concentrations [15], enabling reconstruction of the spatiotemporal evolution of transport states and quantitative examination of concentration-dependent reaction heterogeneity. Independent operando X-ray transmission imaging using LiAsF_6 electrolyte, in which concentration can be directly quantified from transmission contrast, shows qualitative agreement with the reconstructed concentration profiles, supporting the validity of the approach.

This paper is organized as follows. Section 2 describes the experimental procedures and analytical methods. Section 3 presents the reconstructed internal states and their validation. Section 4 discusses the mechanism underlying concentration-dependent spatial charge distribution [15]. Section 5 concludes the study.

2. Materials and Methods

2.1 Operando μ -XAFS Measurements of LIB Composite Cathodes Using LiPF_6 Electrolyte

In this study, operando μ -XAFS measurement data of a model composite cathode reported by Nakamura et al. were analyzed [15]. The model composite electrode used in that study had a structure sandwiched from the top and bottom by an aluminum current collector sheet and a polyimide insulating sheet. This configuration allows electrons to be sufficiently supplied and withdrawn at any position within the electrode, while ionic supply and extraction occur only from the electrode edge. As a result, the charge-discharge reaction in this model electrode proceeds from the electrode edge toward the interior and can locally be regarded as a one-dimensional reaction process (Fig. 1(A1)). Nakamura et al. visualized the one-dimensional propagation of the charge-discharge reaction under operando conditions by irradiating X-rays along the electrode thickness direction, which is perpendicular to the reaction propagation direction.

The composite electrode consisted of LiCoO_2 (hereafter abbreviated as LCO) as the active material, acetylene black (AB) as the conductive additive, and a binder, with a mass ratio of 80:10:10. The electrode thickness was approximately 50 μm . The electrolyte was a mixture of ethylene carbonate (EC) and dimethyl carbonate (DMC) containing dissolved LiPF_6 , and lithium metal foil was used as the negative electrode. Charging was conducted at a constant current density of 6 mA cm^{-2} up to a cutoff voltage of 4.3 V.

Hyperspectral images of the Co K-edge XAFS at each time point during charging (Fig. 1(A2)) were acquired by μ -XAFS measurements. To realize operando measurement, the energy range was restricted to a narrow region near the white line of the absorption edge (7727–7732 eV) (Fig. 1(B1)). The observation area was $600 \times 1200 \mu\text{m}^2$ near the electrode edge (Fig. 1(A1)). The spatial and temporal sampling intervals were 6.5 μm and 300 s (for initial electrolyte concentration 0.3 M) or 240 s (for 1 M and 2 M), respectively. Details of the measurements and sample preparation are described in Ref. [15].

2.2 X-ray Transmission Imaging of LIB Composite Cathodes Employing LiAsF_6 Electrolyte

X-ray transmission imaging measurements were performed on LIB composite electrodes possessing the same structure as the model composite electrodes used by Nakamura et al. [15]. The composite electrodes were fabricated by mixing LiCoO_2 ,

acetylene black, and PolyVinylidene DiFluoride (PVDF) in a weight ratio of 80:10:10 to prepare a composite cathode slurry, which was coated on an aluminum current collector, covered with a polyimide insulating film on the top surface, and dried.

Laminate cells were constructed using the model composite cathode, lithium metal as the anode, and an electrolyte consisting of 1 mol/L LiAsF₆ dissolved in Ethylene Carbonate–Ethyl Methyl Carbonate (EC–EMC) (3:7 v/v%). The cells were charged for 45 minutes at a current of 120 μ A. X-ray transmission images of the composite cathode were acquired by irradiating the electrode with 6.5 keV X-rays (beam size approximately 220 \times 800 μ m) at 1, 5, 25, 35, and 45 minutes after the start of charging.

Because arsenic in the electrolyte salt has a relatively high X-ray absorption coefficient, changes in electrolyte concentration significantly affect the contrast of X-ray transmission images. Therefore, the electrolyte concentration distribution within the electrode was evaluated from the difference in brightness between each X-ray transmission image acquired during charging and the image obtained before charging in the same observation region.

2.3 SOC Evaluation Based on PTE and the Two-Phase Reaction Region

In the previous study by Nakamura et al., SOC maps were constructed from the acquired XAFS hyperspectral images according to the procedure described below [15]. In the present study, this method was adopted for SOC evaluation.

Figure 1(B1) shows an example of a Co K-edge XAFS spectrum at a given spatiotemporal point. In LCO, it is known that as lithium is extracted, the valence state of Co increases, and correspondingly, the peak top energy (PTE) of the Co K absorption edge shifts toward higher energy.

In this study, the PTE was extracted from the XAFS spectrum at each spatiotemporal point, and the SOC at each point was evaluated using a quadratic regression curve representing the PTE–SOC relationship obtained from standard samples (Fig. 1(B2)). However, as shown in Fig. 1(B2), in the region where SOC exceeds a threshold x_{th} , the change in PTE accompanying lithium extraction becomes extremely small, making

it difficult to uniquely determine SOC. This behavior of the PTE is considered to originate from the fact that lithium insertion/extraction in LCO proceeds as a two-phase reaction in the SOC range of approximately 0.75–0.94 [37,38].

In this study, this region is referred to as the two-phase reaction region. For $x > x_{th}$, SOC is regarded as not uniquely determinable and is assigned a representative value of 1. In contrast, for $x < x_{th}$, SOC is evaluated based on the regression curve. By this method, SOC maps at each time point, as shown in Fig. 1(B3), are constructed.

2.4 Overview of the Analysis Pipeline

In this study, we constructed an analysis pipeline to quantitatively extract material transport and charge-transfer processes coupled with charge-discharge reactions from XAFS hyperspectral data obtained by operando microspectroscopy of LIB composite cathodes. As a proof-of-concept model case, we analyzed Co K-edge XAFS spectral data of the above-mentioned LIB composite cathodes acquired by operando μ -XAFS measurements [15].

Figure 1(C) presents the overall workflow of the proposed pipeline. The pipeline takes as input the SOC maps constructed using the conventional method by Nakamura et al. The pipeline comprises two main components:

- (i) a three-layer NN that resolves ambiguities in the two-phase reaction region where SOC cannot be uniquely determined, and
- (ii) a Kirchhoff-based Markov random field (Kirchhoff MRF) that quantitatively estimates material transport processes based on the inferred SOC distribution.

In the NN module, physics-informed regularization is introduced to enforce spatial continuity of SOC and current conservation, enabling stable reconstruction of the spatiotemporal SOC distribution, including the two-phase reaction region. The inferred SOC dynamics are then supplied to the Kirchhoff MRF, which integrates Kirchhoff's current and voltage laws, Ohm's law, and interfacial reaction kinetics within a simplified porous electrode model. This probabilistic framework allows consistent estimation of internal physical quantities constrained by both electrochemical law and the SOC distribution.

This integrated approach enables quantitative inference of otherwise inaccessible internal state variables, including solid–liquid interfacial current, ionic current in the electrolyte, electrolyte potential distribution, and effective ionic conductivity.

Detailed descriptions of each component are provided in the following sections.

2.5 Physics–regularized NN for SOC estimation in the two–phase region

With the method described in Section 2.3, SOC in the two–phase reaction region cannot be uniquely determined, which limits quantitative analysis of lithium–ion transport processes. To overcome such difficulties, we introduce spatial continuity of SOC and current conservation as regularization constraints, and regress the spatiotemporal SOC distribution using a three–layer NN under physics–informed regularization.

The data structure of the SOC spatiotemporal map is shown in Fig. 2(A). We define the SOC at time t , at pixel index i in the z –direction corresponding to the direction from the electrode edge toward the center, i.e., the direction in which charging proceeds, and at pixel index j in the lateral direction as $x_{i,j}(t)$. Let the numbers of pixels in the z – and lateral directions be N and M , respectively, and the total number of frames be L . Because the reaction progression considered in this study is one–dimensional, we treat the lateral pixel index j as an ensemble sample index, and focus on the z –direction pixel index i and time t in the following.

The structure of the introduced three–layer NN is shown in Figs. 2(B1) and 2(B2). In Fig. 2(B1), the input layer consists of cells In_i corresponding to each pixel index i in the z –direction, and outputs time t . The hidden layer has K cells $M_{1,i}$ to $M_{K,i}$ for each pixel index i , and uses a sigmoid activation function. The output layer consists of cells O_i corresponding to each pixel index i , and outputs the estimated SOC $y_{O,i}(t)$ without using an activation function. Here, $\textcircled{1}$ is a cell that outputs the constant 1 and corresponds to the bias term. Accordingly, the input–output relationship of the NN for pixel index i is given by Eq. (1):

$$y_{O,i}(t) = \sum_{k=1}^K b_{k,i} \sigma(a_{k,1,i} - a_{k,2,i} t) + b_{K+1,i}. \quad (1)$$

Here, $\sigma(x)$ is the sigmoid function defined as $\sigma(x) = (1 + \tanh(x))/2$. The parameters $\{a_{1,1,i}, a_{1,2,i}\}$ to $\{a_{K,1,i}, a_{K,2,i}\}$ represent the connection weights to the cells $M_{1,i}$ to $M_{K,i}$, and $\{b_{1,i}, \dots, b_{K,i}, b_{K+1,i}\}$ are the connection weights to the cell O_i . In this study, because many reaction curves can be described by hyperbolic functions, we adopted the sigmoid function as the activation function.

The time derivative of the NN output $y_{O,i}(t)$ corresponds to the current associated with lithium deintercalation/intercalation in LCO at pixel index i , and is expressed by Eq. (2):

$$I_{O,i}(t) = \frac{S}{2} \sum_{k=1}^K \frac{a_{k,2,i} b_{k,i}}{\cosh^2(a_{k,1,i} - a_{k,2,i} t)}. \quad (2)$$

Here, S is a scaling factor that determines the current magnitude; details are given in Appendix A.1.

In addition, the component shown in Fig. 2(B2) estimates the liquid-phase current at time t at the position $i = N + 1$ outside the observation points in the z -direction; similarly, it is represented by a three-layer NN as Eq. (3):

$$J_{O,bc}(t) = \sum_{k=1}^K b_{k,bc} \sigma(a_{k,1,bc} - a_{k,2,bc} t) + b_{K+1,bc}. \quad (3)$$

For training the NNs in Figs. 2(B1) and 2(B2), we optimize the connection weights by steepest descent with respect to the loss function defined in Eq. (4):

$$\begin{aligned}
\mathcal{L} = & \frac{1}{2M} \sum_{i,j,t \in \{x_{i,j}(t) \neq 1\}} (x_{i,j}(t) - y_{o,i}(t))^2 \\
& + \frac{1}{2M(1 - x_{th})} \sum_{i,j,t \in \{x_{i,j}(t) = 1\}} \int_{x_{th}}^1 (x - y_{o,i}(t))^2 dx \\
& + \frac{A}{2} \sum_t \left(J_c - \sum_i I_{o,i}(t) - J_{o,bc}(t) \right)^2 + \frac{B}{2} \sum_{i,t} (y_{o,i+1}(t) - y_{o,i}(t))^2 \\
& + \frac{C}{2} \sum_{i,t \in \{y_{o,i}(t) \leq 0.5\}} (0.5 - y_{o,i}(t))^2 + \frac{C}{2} \sum_{i,t \in \{y_{o,i}(t) \geq 1\}} (1 - y_{o,i}(t))^2. \tag{4}
\end{aligned}$$

The first term is a squared-error term for data fitting in the range $0.5 < x < x_{th}$. The second term accounts for the fact that SOC is not uniquely determined in the region $x > x_{th}$, and is a squared-error term derived under the assumption that the data follow a uniform distribution. The summation over the lateral index j corresponds to the operation of taking the ensemble average.

The third and subsequent terms are physics-informed regularization terms that ensure the physical validity of the SOC estimates. The third term constrains the sum of the current corresponding to lithium deintercalation/intercalation from LCO at each point and the liquid-phase current at $i = N + 1$ outside the observation points in the z -direction, to match the experimental charging current density J_c (mA/cm²). The fourth term enforces continuity of SOC estimates between adjacent points in the z -direction. The fifth and sixth terms impose strong penalties when $y_{o,i}(t)$ falls below 0.5 or exceeds 1, respectively.

Using the method of steepest descent, we determine the connection weights and bias terms that minimize the loss function defined in Eq. (4), thereby training the network. The red lines shown in Figs. 2(B1) and 2(B2) represent the signal flow of error backpropagation during learning. During training, in addition to the error between the SOC data $x_{i,k}(t)$ and the NN output $y_{o,i}(t)$, the gradients of the physics-informed regularization terms—such as current conservation and spatial continuity—are simultaneously propagated. Each connection weight and bias term is updated according to these gradient signals.

Figure 3(A) shows the estimated spatiotemporal SOC distributions for samples with initial electrolyte concentrations of 0.3 M, 1 M, and 2 M. The charging current density was fixed to the experimental value $J_c = 6$ mA/cm², and the threshold for the two-

phase reaction region was set to $x_{\text{th}} = 0.85$. We also examined cases where the threshold was changed to $x_{\text{th}} = 0.9$, and found no essential differences in the estimated SOC distributions, confirming that the proposed method is robust with respect to the threshold setting. The procedures used to determine the regularization parameters A , B , and C , as well as the number of hidden units K , and their specific values are provided in Appendix A.3.

2.6 Kirchhoff MRF

In this study, we introduce a **Kirchhoff Markov random field** (Kirchhoff MRF) in which relationships derived from Kirchhoff's laws are incorporated into the equivalent circuit of a porous electrode model of secondary batteries, and estimate lithium-ion transport dynamics from the spatiotemporal SOC map.

Figure 4(A) shows the equivalent circuit based on the porous electrode model used in this study. The lithium deintercalation/intercalation reaction in LCO at time t and at pixel index i in the z -direction is represented as charging/discharging of a capacitor. We define the **LCO current** corresponding to the current entering/leaving the capacitor as $I_{LCO,i}(t)$, and the **open-circuit voltage (OCV)** of LCO corresponding to the potential difference of the capacitor as $V_{LCO,i}(t)$. We also define the current flowing through the solid-liquid interface as $I_i(t)$, the current flowing in the liquid phase along the z -direction as $J_i(t)$, the liquid-phase potential as $V_i(t)$, and the liquid-phase ohmic resistivity as $r_i(t)$. In this model, the solid-phase potential is taken as the reference (ground) to define the polarity of potential, and the current direction is defined to be positive along the arrow directions shown in Fig. 4(A).

The LCO potential $V_{LCO,i}(t)$ and current $I_{LCO,i}(t)$ are provided from the output of the physics-regularized three-layer NN in the preceding stage of the analysis pipeline. Specifically, we assign $I_{LCO,i}(t)$ to $I_{O,i}(t)$ in Eq. (2), which is given by the time derivative of the NN output $y_{O,i}(t)$ (the SOC estimate). We obtain $V_{LCO,i}(t)$ by applying the OCV curve given by Eq. (A.6) in the Appendix to the NN output $y_{O,i}(t)$.

The spatiotemporal distributions of $I_{LCO,i}(t)$ and $V_{LCO,i}(t)$ calculated from the estimated SOC maps for samples with initial electrolyte concentrations of 0.3 M, 1 M, and 2 M (Fig. 3(A)) are shown in Figs. 3(B) and 3(C), respectively.

In this model, we assume that the solid-phase resistivity is sufficiently smaller than the liquid-phase resistivity and that the diffusion process is quasi-static, so that ionic transport obeys Ohm's law. Furthermore, the relationship between the interfacial current $I_i(t)$ and the interfacial potential difference $V_i(t) - V_{LCO,i}(t)$ follows the Butler-Volmer (BV) equation [39], assuming symmetric anodic and cathodic reactions as shown in Fig. 3(B), and is given by Eq. (5):

$$I_i(t) = BV(V_i(t) - V_{LCO,i}(t)) = 2i_0 \sinh\left(\frac{F(V_i(t) - V_{LCO,i}(t))}{2RT}\right). \quad (5)$$

Here, F is Faraday's constant, R is the gas constant, and T is temperature. The parameter i_0 represents the exchange current associated with an electrode subregion of cross-sectional area s (cm^2). In this study, the exchange current density is assumed to be constant and independent of spatiotemporal variations in electrolyte concentration. For a subregion with $s = 6.5 \times 10^{-3} \text{cm}^2$, the corresponding exchange current i_0 was set to 1.8040×10^{-6} , 3.2937×10^{-6} , and $4.6580 \times 10^{-6} \text{mA}$ for initial electrolyte concentrations of 0.3 M, 1 M, and 2 M, respectively. The procedure used to estimate these values is described in Appendix A.1.

In addition, V_c and J_c in Fig. 4(A) represent the charging voltage and charging current, respectively, and are known quantities. The liquid-phase current $J_{N+1}(t)$ at $i = N + 1$, located outside the observation points along the z -direction, is estimated from $J_{O,bc}(t)$, which is determined simultaneously in the SOC estimation process in the previous section. Based on these known quantities, we define the boundary conditions of the equivalent circuit as Eq. (6):

$$\begin{aligned} J_0(t) &= J_c, & J_{N+1}(t) &= J_{O,bc}(t), \\ V_0(t) &= V_c, & V_{N+1}(t) &= V_N(t) + r_N(t)J_N(t), \\ r_0(t) &= r_1(t), & r_{N+1}(t) &= r_N(t). \end{aligned} \quad (6)$$

Here, the boundary condition for the liquid-phase ohmic resistivity is a free-end boundary condition. The boundary condition for the liquid-phase potential is imposed by assuming that the potential gradient at $i = N$ and $i = N + 1$ is identical, that is, $V_N(t) - V_{N-1}(t) = V_{N+1}(t) - V_N(t) = r_N(t)J_N(t)$.

To estimate the internal state variables consistent with these governing relationships, we construct a Hamiltonian corresponding to the evaluation function in Eq. (7), in which Kirchhoff's first and second laws and the BV equation as constraints.

$$\begin{aligned}
\mathcal{H} = & \beta \sum_{t=1}^L \sum_{i=1}^N (I_i(t) - I_{LCO}(t))^2 + \eta \sum_{t=1}^L \sum_{i=1}^N (V_i(t) + V_{LCO}(t) - BV^{-1}(I_i(t)))^2 \\
& + \delta \sum_{t=1}^L \sum_{i=1}^N (J_{i+1}(t) - J_i(t) + I_i(t))^2 \\
& + \gamma \sum_{t=1}^L \sum_{i=1}^N (V_{i+1}(t) - V_i(t) + r_i(t)I_i(t))^2 \\
& + \phi \sum_{t=1}^L \sum_{i=1}^N (r_{i+1}(t) - r_i(t))^2 + \psi \sum_{t=1}^L \sum_{i=1}^N (r_i(t) - \bar{r})^2. \quad (7)
\end{aligned}$$

The first term represents the residual between $I_{LCO,i}(t)$ estimated by the three-layer NN and the interfacial current $I_i(t)$, and corresponds to the likelihood. The second term represents current conservation between the interfacial current $I_i(t)$ and the liquid-phase current $J_i(t)$, i.e., Kirchhoff's first law. The third term includes the inverse function of the BV equation in Eq. (5) and represents the nonlinear current-voltage characteristics at the solid-liquid interface. The potential including this term obeys Kirchhoff's second law. Because this term includes $V_{LCO,i}(t)$ obtained from the SOC estimated by the three-layer NN, it can also be regarded as a likelihood term for the potential. The fourth term includes the ohmic voltage loss in the lithium-ion transport process along the z -direction, and the potential including this term also obeys Kirchhoff's second law. The fifth term is a regularization term imposing spatial continuity of the liquid-phase resistivity, and the sixth term is a regularization term requiring that $r_i(t)$ does not deviate substantially from the reference resistivity \bar{r} determined by the initial electrolyte concentration.

The Hamiltonian is constructed as a weighted linear combination of these terms with hyperparameters $\beta, \delta, \eta, \gamma, \phi, \psi$. Because the Hamiltonian includes the nonlinear BV equation, it is not a quadratic function. The inverse BV function is used in the third term to numerically stabilize Gibbs sampling provided in Appendix A.2.

Based on this Hamiltonian, we construct the Kirchhoff MRF as the high-dimensional probability distribution given by Eq. (8):

$$\begin{aligned}
P(J, I, V, r, I_{LCO}, V_{LCO} | \beta, \delta, \eta, \gamma, \phi, \psi, \bar{r}) = & P(I_{LCO} | I, \beta) \cdot P(V_{LCO} | V, I, \eta) \\
& \cdot P(I | J, \delta) \cdot P(J, V | r, \gamma) \cdot P(r | \phi, \psi, \bar{r}). \quad (8)
\end{aligned}$$

Each term in Eq. (8) is composed of the conditional probability densities in Eqs. (9)–(13):

$$P(I_{LCO} | I, \beta) \propto \prod_{t=1}^T \exp \left(-\beta \sum_{i=1}^N (I_i(t) - I_{LCO,i}(t))^2 \right), \quad (9)$$

$$P(V_{LCO} | V, I, \eta) \propto \prod_{t=1}^T \exp \left(-\eta \sum_{i=1}^N (V_i(t) + V_{LCO,i}(t) - BV^{-1}(I_i(t)))^2 \right), \quad (10)$$

$$P(I | J, \delta) \propto \prod_{t=1}^T \exp \left(-\delta \sum_{i=1}^N (J_{i+1}(t) - J_i(t) + I_i(t))^2 \right), \quad (11)$$

$$P(J, V | r, \gamma) \propto \prod_{t=1}^T \exp \left(-\gamma \sum_{i=1}^N (V_{i+1}(t) - V_i(t) + r_i(t)I_i(t))^2 \right), \quad (12)$$

$$P(r | \phi, \psi, \bar{r}) \propto \prod_{t=1}^T \exp \left(-\phi \sum_{i=1}^N (r_{i+1}(t) - r_i(t))^2 - \psi \sum_{i=1}^N (r_i(t) - \bar{r})^2 \right). \quad (13)$$

The dependency structure among the state variables is organized as the hierarchical Bayesian structure shown in Fig. 3(C). Because we assume a quasi-static reaction process, the states at each time t are regarded as probabilistically independent. Under the given boundary conditions (Eq. (6)), we sampled the marginal posterior distributions using Gibbs sampling. Details of the Gibbs sampling algorithm and the hyperparameters used are provided in Appendices A.2 and A.3.

3. Results

3.1 Estimation of internal battery states from operando microscopic spectroscopy data

In this section, we apply the proposed analysis pipeline shown in Fig. 1(C) to operando μ -XAFS hyperspectral datasets acquired for three LIB composite cathode samples with different initial electrolyte concentrations (LiPF_6 : 0.3 M, 1 M, and 2 M), and elucidate the spatiotemporal dynamics of internal battery states during charging.

Under the conditions described in Section 2.1, the charging current density was fixed at $J_c = -6 \text{ mA/cm}^2$, and data up to the point where the charging voltage reached $V_c = -4.3 \text{ V}$ were analyzed. Note that in this model the solid phase is taken as ground and the liquid-phase potential is defined relative to it; the positive direction of current is also defined as the direction indicated by the arrows in Fig. 4(A). Accordingly, V_c and I_c take negative values.

By applying the methods described in Sections 2.3 and 2.5 to the Co K-edge XAFS spectra obtained by operando microscopic measurements, we estimated the spatiotemporal SOC distribution including the two-phase reaction region (Fig. 3(A)), and calculated the lithium deintercalation/intercalation current I_{LCO} and the OCV V_{LCO} in LCO (Figs. 3(B) and 3(C)). Furthermore, by applying the Kirchhoff-MRF, we estimated the spatiotemporal distributions of the solid-liquid interfacial current I , liquid-phase current J , liquid-phase potential V , and the liquid-phase conductivity $s = 1/r$, defined as the reciprocal of the liquid-phase ohmic resistivity r .

Figure 5 shows the temporal evolution of the spatial distributions of these estimated internal states. In each panel, for better visualization of the spatial profiles at each time point, the reference value is sequentially shifted in the vertical direction, and the corresponding time is indicated on the right. The red line denotes the reference value at each time, and its numerical value is also shown. In the panels for the current J and potential V , the light-blue dashed line indicates the values of these states on the electrode-interior side, and the corresponding numerical values are also shown.

3.1.1 Case of initial electrolyte concentration 0.3 M

Figure 5(A) shows the estimation results for the sample with an initial electrolyte concentration of 0.3 M. Focusing on the distribution of the solid-liquid interfacial current I , a negative dip is observed to move from the electrode edge (distance 0) toward the interior as time progresses, as indicated by the gray arrows in the figure. This negative current dip corresponds to Li deintercalation from LCO, and its motion reflects the progression of the charging reaction from the electrode edge into the interior.

In the distribution of the liquid-phase conductivity s , an increase in conductivity is observed near the electrode edge immediately after the start of charging, and this high-conductivity region expands inward with time. Simultaneously with this

conductivity increase, the spatial gradient of the liquid-phase potential V gradually becomes gentler, suggesting a reduction in ohmic loss associated with ionic transport in the liquid phase.

These results indicate that, as the ohmic loss decreases, the electrode-edge potential that drives the reaction is sufficiently transmitted into the electrode interior, thereby allowing the charging reaction to propagate inward. Moreover, the gradual propagation of the reaction from the electrode edge, which serves as the ion outlet, suggests that ionic transport may play a dominant role in governing the overall reaction kinetics in this electrode. This behavior implies that electronic conduction through the conductive additive or active material, as well as interfacial charge-transfer reactions, are unlikely to be the primary rate-limiting steps under the present conditions.

These results indicate that, as the ohmic loss decreases, the electrode-edge potential driving the reaction is effectively transmitted into the electrode interior, thereby enabling inward propagation of the charging reaction. Furthermore, the gradual propagation of the reaction from the electrode edge, which serves as the ion outlet, suggests that ionic transport plays a dominant role in governing the overall reaction kinetics in this electrode. This behavior is consistent with a scenario in which electronic conduction through the conductive additive or active material, as well as interfacial charge-transfer reactions, are not the primary rate-limiting processes under the present conditions.

3.1.2 Cases of initial electrolyte concentration 1 M and 2 M

Figures 4(B) and 4(C) show the estimation results for samples with initial electrolyte concentrations of 1 M and 2 M, respectively. Under these conditions, behavior contrasting with the 0.3 M case was observed.

In the distribution of the solid-liquid interfacial current I , the negative current dip remains near the electrode edge and no clear inward migration with time is observed, as indicated by the gray arrows. That is, the charging reaction is localized near the electrode edge and its progression into the interior is suppressed.

Moreover, the liquid-phase conductivity σ decreases monotonically with time after the start of charging, and no local conductivity increase such as that observed in the 0.3 M case is detected. Correspondingly, the spatial gradient of the liquid-phase

potential V increases, indicating an increase in ohmic loss associated with ionic transport in the liquid phase.

Taken together, these results suggest that, for initial electrolyte concentrations of 1 M and 2 M, increased ohmic loss in the liquid phase hinders potential transmission into the electrode interior, thereby confining the charging reaction to the vicinity of the electrode edge.

3.2 Comparison between estimated electrolyte concentration distributions and operando measurements

In this section, we estimate the electrolyte concentration distribution in the electrode from the spatiotemporal distribution of the liquid-phase conductivity s estimated in the previous section, and directly validate its plausibility using operando measurements.

3.2.1 Concentration estimation based on the conductivity–electrolyte concentration relationship

A previous study [40,41] reported an empirical relationship between the liquid-phase conductivity and electrolyte concentration in LIB cathodes employing a LiPF_6 electrolyte (Appendix Eq. (A.7)). Figure 6(A) shows this relationship as a function of salt concentration. The conductivity exhibits a non-monotonic behavior: it takes a maximum around ~ 1 M and decreases toward both lower and higher concentrations.

In this study, we estimated the electrolyte concentration distribution in the electrode at each time by substituting the estimated conductivity s (Fig. 5) into this relationship. Because this relationship yields two concentration solutions for a single conductivity value, we selected the solution that preserves temporal continuity from the initial electrolyte concentration.

Figures 6(B)–6(D) show the temporal evolution of the estimated electrolyte concentration distributions for initial LiPF_6 concentrations of 0.3 M, 1 M, and 2 M, respectively, together with the corresponding changes in charging voltage and charging capacity.

3.2.2 Characteristics of the estimated concentration distributions

For the initial concentration of 0.3 M in Fig. 6(B), a sharp concentration profile forms near the electrode edge immediately after the start of charging, and the profile broadens toward the interior with time. This progression of the concentration distribution is consistent with the inward propagation of the charging reaction shown in Section 3.1.1. It took approximately 105 min for the charging voltage to reach the upper limit, during which the charging capacity reached approximately 25 mAh/g. No saturation of the concentration or charging voltage was observed in the late stage of charging.

In contrast, for initial concentrations of 1 M and 2 M in Figs. 6(C) and 6(D), a concentration distribution spreading across the entire electrode forms immediately after charging starts, followed by an overall increase in concentration. The charging voltage reached the upper limit after approximately 64 min for 1 M and approximately 28 min for 2 M, and the charging capacities were lower than that for 0.3 M in both cases. No saturation of the concentration or charging voltage was observed in the late stage of charging.

3.2.3 Comparison with operando X-ray transmission measurements

To validate the estimation results, we directly measured the electrolyte concentration distribution by operando X-ray transmission imaging for a sample electrode of the same structure using a LiAsF₆ electrolyte instead of LiPF₆. LiAsF₆ was employed because arsenic, with its large atomic weight, increases X-ray absorption, enabling quantitative evaluation of electrolyte concentration changes as contrast variations in the X-ray transmission images. In this experiment, the initial electrolyte concentration was set to 1 M, and the cell was charged for 45 min under a charging current density of 6 mA/cm². Experimental details are provided in Section 2.2. Figure 7 shows the temporal evolution of the electrolyte concentration distribution evaluated from the difference between transmission images acquired before and after charging, together with the corresponding changes in charging voltage and charging capacity.

When LiAsF₆ was used, a concentration distribution spreading over the entire electrode formed immediately after the start of charging, followed by an increase in concentration throughout the electrode. This behavior qualitatively agrees with the

temporal changes in the electrolyte concentration distributions estimated for the 1 M and 2 M LiPF₆ conditions in Figs. 6(C) and 6(D).

On the other hand, in the LiAsF₆ case, the concentration increase tended to saturate in the late stage of charging (35–45 min). The charging voltage shown in the right panel likewise exhibited saturation in the late stage. Such saturation behavior was not observed for the LiPF₆ electrolyte cases in Figs. 6(C) and 6(D).

Thus, except for the saturation behavior in the late stage of charging, the temporal evolution of the electrolyte concentration distributions estimated by the proposed method under these two conditions is consistent with the results obtained by direct operando measurements.

4. Discussion

4.1 Validity of the estimated electrolyte concentration distributions

In this study, the spatiotemporal distribution of the liquid-phase conductivity estimated from the operando μ -XAFS dataset was converted into an electrolyte concentration distribution based on the conductivity–electrolyte concentration relationship shown in Fig. 6(A). The estimated results for initial electrolyte concentrations of 1 M and 2 M qualitatively agree with the directly measured results obtained by operando X-ray transmission imaging using a LiAsF₆ electrolyte (Figs. 6(C), 6(D) and 7). Therefore, at least for the concentration–distribution behavior from the early to middle stages of charging, the present approach is considered to provide an electrochemically reasonable estimation.

Because the anion species differs between LiPF₆ and LiAsF₆, their transport properties may differ due to differences in diffusion coefficients and solvation structures. However, it is known that diffusion coefficients generally decrease as electrolyte concentration increases, and the differences originating from the anion species become relatively small [43]. The agreement between the estimated results and the

direct measurements in the electrolyte concentration regime of ≥ 1 M suggests that the proposed method appropriately captures the dominant reaction dynamics.

The saturation of electrolyte concentration and charging voltage observed in the late stage of charging in the direct measurements was not captured under either the 1 M or 2 M initial electrolyte concentration conditions. This is likely because the cutoff voltage was set to 4.3 V and the measurement was terminated before saturation occurred.

Contrary, for the initial electrolyte concentration of 0.3 M, the electrolyte was estimated to diffuse from the electrode edge toward the electrode center. This electrolyte-diffusion behavior is consistent with the situation in which the charging reaction propagates toward the electrode center, and thus the present estimation is considered reasonable. Notably, such behavior was observed for the first time in this study, and verification of its validity remains an issue for future work.

4.2 Dependence of the charging reaction mode on electrolyte concentration and its mechanism

In the study by Nakamura et al. [15], the concentration-dependent reaction behavior was qualitatively attributed to electrolyte concentration modulation within the electrode, although the spatiotemporal evolution of the electrolyte concentration was not directly verified. In contrast, the present framework enables probabilistic reconstruction of electrolyte conductivity and concentration distributions from operando spectroscopic data, providing a quantitative basis for evaluating this hypothesis.

For an initial electrolyte concentration of 0.3 M, the charging reaction propagates from the electrode edge toward the interior, whereas for 1 M and 2 M it remains confined near the electrode edge. This behavior originates from the non-monotonic dependence of ionic conductivity on electrolyte concentration as seen in Fig. 6A. Under low-concentration conditions (0.3 M), the initially low conductivity restricts the reaction to the electrode edge. As charging proceeds, local concentration increases and diffuses inward; because the system remains below 1 M, conductivity increases with concentration, reducing liquid-phase ohmic loss and enabling deeper potential

penetration into the electrode. This positive feedback between concentration enhancement and conductivity promotes inward reaction propagation.

In contrast, at 1 M and 2 M, the electrolyte resides in a regime where further concentration changes reduce ionic conductivity. The resulting increase in liquid-phase ohmic loss suppresses potential transmission into the electrode interior, thereby confining the reaction to the electrode edge.

4.3 Validity and limitations of the model

The Kirchhoff MRF used in this study was constructed on the basis of an equivalent circuit derived from a simplified porous electrode model, with emphasis on ensuring that the latent states are uniquely determined from the spatiotemporal SOC distribution and on computational tractability.

The assumption that the solid-phase resistance is negligible compared with the liquid-phase resistance is reasonable for thin-film electrodes containing sufficient conductive additive, but it should be reconsidered for thick electrodes or low-conductivity materials. The assumption that diffusion is quasi-static and that ionic transport follows Ohm's law is also reasonable under the charging conditions of this study, but extensions may be required under high-rate conditions or in situations where steep concentration gradients form. Furthermore, the interfacial reaction was assumed to follow a symmetric Butler-Volmer equation; variations in the interfacial exchange current depending on the Li concentration in LCO or the electrolyte concentration, as well as interfacial inhomogeneity, were not explicitly considered.

These assumptions are sufficient for capturing overall trends in the spatiotemporal dynamics of latent states; however, further model refinement is necessary to improve quantitative accuracy.

4.4 Challenges in hyperparameter estimation

In the proposed Kirchhoff MRF of Eq. (7), multiple hyperparameters ($\beta, \eta, \delta, \gamma, \phi, \psi$) were introduced to control the contributions of the likelihood term and various regularization terms. Because these hyperparameters strongly affect the consistency between the observed data and the physical model, as well as the spatial and temporal

smoothness of the estimated latent states, appropriate settings are a key factor governing the quantitative reliability and stability of the estimation.

In this study, as described in Appendix A.3, empirically reasonable values were selected while considering numerical stability of the estimation. However, a framework for automatic hyperparameter estimation from the observed data was not introduced. Therefore, when applying this method to different material systems or measurement conditions, re-tuning of the hyperparameters may be required.

In future work, the generality and reproducibility of the proposed method could be further improved by integrating a unified hyperparameter estimation framework into the analysis pipeline, such as marginal likelihood maximization or a hierarchical Bayesian formulation incorporating hyperpriors. In addition, systematically evaluating how each hyperparameter influences the estimation of physical quantities via sensitivity analysis is an important future task.

4.5 Further development of the proposed method

In this study, we analyzed operando microscopic measurement data for a reaction process in which the charging reaction progresses along a one-dimensional direction. However, the present analysis method is readily extendable to higher-dimensional spaces, and it should be applicable to the analysis of reaction processes that progress in multiple spatial dimensions.

In the proposed analysis pipeline, SOC estimation by the physics-regularized three-layer NN and ion-transport dynamics estimation by the Kirchhoff MRF are optimized separately. On the other hand, it is also possible to perform these optimization procedures simultaneously under a single objective function by leveraging recent deep learning methods [43]. Such joint optimization may enable SOC estimation—including the two-phase reaction region—based on the porous electrode model, and further improvements in estimation accuracy are anticipated.

The proposed analysis pipeline is not specific to a particular material system or measurement technique; rather, it can be positioned as a general framework that integrates operando microscopic spectroscopic data with an equivalent-circuit model describing electrochemical reactions. Therefore, the method is not limited to lithium-

ion secondary batteries and can potentially be extended to the analysis of diverse measurement datasets for other rechargeable battery systems.

5. Conclusion

In this study, we developed a physics-integrated analysis pipeline that quantitatively estimates internal electrochemical states of LIB composite cathodes from operando μ -XAFS hyperspectral data. By combining (i) a physics-regularized three-layer NN for resolving SOC distributions in the two-phase reaction region and (ii) a Kirchhoff MRF incorporating Kirchhoff's laws, Ohm's law, and the Butler-Volmer equation, we achieved simultaneous inference of interfacial current, ionic current, electrolyte potential, and effective ionic conductivity.

Application of the proposed framework to electrodes with different initial electrolyte concentrations (0.3, 1, and 2 M LiPF_6) revealed electrolyte-concentration-dependent reaction propagation modes. Under low-concentration conditions (0.3 M), local conductivity enhancement and increased solid-phase resistance promoted inward propagation of the charging reaction. In contrast, at higher concentrations (1 and 2 M), increased ohmic losses suppressed potential transmission into the electrode interior, leading to reaction localization near the electrode edge. The inferred electrolyte concentration distributions were qualitatively consistent with independent operando X-ray transmission imaging using LiAsF_6 electrolyte, supporting the physical plausibility of the proposed approach.

Although the present model relies on simplified assumptions regarding transport and interfacial kinetics, it successfully captures the essential spatiotemporal trends of coupled reaction-transport dynamics. The proposed framework is not limited to LIB systems and provides a general methodology for integrating operando spectroscopic data with physics-based probabilistic modeling. Future developments, including systematic hyperparameter estimation and model refinement, are expected to further improve quantitative accuracy and expand applicability to broader electrochemical systems.

Appendix

A.1 Physical parameters of the sample electrode

The model electrode is a square of $1\text{ cm} \times 1\text{ cm}$ with a thickness of $46\text{ }\mu\text{m}$. The theoretical specific capacity of LCO for the full delithiation reaction, $\text{Li}_{1.0}\text{CoO}_2 \rightarrow \text{CoO}_2$ is 274 mAh/g [44]. Given that the electrode contains 6.736 mg of LCO, the maximum capacity of the electrode is $274 \times 6.736 \times 10^{-3}\text{ mAh}$. Therefore, letting $s\text{ (cm}^2\text{)}$ denote the area of an electrode subregion and x the SOC in that subregion, the charge $q\text{ (mAh)}$ stored in the subregion is given by Eq. (A.1):

$$q = s(1 - x) \times 274 \times 6.736 \times 10^{-3}. \quad (\text{A.1})$$

Let Δt (hour) be the measurement time interval in operando measurements. Then, by considering Eq. (A.1) together with the electrode thickness, the coefficient S in Eq. (2) can be determined by Eq. (A.2):

$$S = \frac{s \times 274 \times 6.736 \times 10^{-3}}{46 \times 10^{-4} \times \Delta t}. \quad (\text{A.2})$$

Next, we estimate the exchange current density at the solid–liquid interface. The active–material surface area per unit volume, $a\text{ (cm}^2\text{/cm}^3\text{)}$, can be evaluated following Ref. [45] as

$$a = \frac{3(2 - \varepsilon_{\text{else}})}{R_s}. \quad (\text{A.3})$$

Here, R_s is the LCO particle radius, and $\varepsilon_{\text{else}}$ is the volume fraction of components other than LCO in the electrode. For the present electrode, $R_s = 6.0\text{ }\mu\text{m}$ and $\varepsilon_{\text{else}} = 0.716$, yielding $a = 1419\text{ cm}^2\text{/cm}^3$. Therefore, the active–material surface area $s_{\text{AM}}\text{ (cm}^2\text{)}$ in an electrode subregion of area s , taking the electrode thickness into account, is expressed as

$$s_{\text{AM}} = 46 \times 10^{-4} \times s \times a = 6.53 s. \quad (\text{A.4})$$

Using Eq. (A.5)—obtained by multiplying the Newman–model expression for the interfacial exchange current density by the active–material surface area s_{AM} in Eq. (A.4)—we evaluate the exchange current i_0 appearing in the Butler–Volmer equation (Eq. (5)) for an electrode subregion of cross–sectional area $s\text{ (cm}^2\text{)}$:

$$i_0 = 0.1 \cdot s_{AM} \cdot k \cdot c_{salt}^{0.5} \cdot (c_{max} - c)^{0.5} \cdot c^{0.5}. \quad (A.5)$$

Here, k is the reaction-rate constant; c_{salt} is the electrolyte salt concentration [mol/m³]; c_{max} is the Li concentration in LCO at stoichiometry [mol/m³]; and c is the Li concentration in LCO [mol/m³]. This expression indicates that the exchange current density depends on both the electrolyte salt concentration and the Li concentration in LCO. In this study, we treat the exchange current density i_0 as a constant. To this end, the parameters are approximated as $k = 5.0 \times 10^{-11}$, $c_{max} = 52752 \text{ mol/m}^3$, $c = 40000 \text{ mol/m}^3$ corresponding to the median of the variation range (32000–52752 mol/m³). The reaction-rate constant follows the value adopted in the NEDO RISING battery development project, while the remaining parameters are estimated from Ref. [44]. The electrolyte salt concentration c_{salt} is approximated by the initial electrolyte concentration. Accordingly, different i_0 values described in the main text are used for initial electrolyte concentrations of 0.3 M, 1 M, and 2 M.

The OCV curve $E(x)$ of LCO used in this study is given by Eq. (A.6), obtained by regression of experimental data [46]:

$$E(x) = \begin{aligned} & 2.162 + 0.471 \tanh(2.766 - 5.703x) \\ & + 2.060 \tanh(78.24 - 77.56x) + 0.142 \tanh(4.123 - 8.023x). \end{aligned} \quad (A.6)$$

Here, x is the SOC of LCO.

In addition, the relationship between ionic conductivity and salt concentration in the positive electrode employing LiPF₆ as the electrolyte salt (Fig. 5(A)) follows the empirical equation reported in previous studies [40, 41], Eq. (A.7):

$$k_{eff} = \epsilon^{1.5} \cdot 1000(-0.7222 c_{salt}^4 + 6.0577 c_{salt}^3 - 19.045 c_{salt}^2 + 22.614 c_{salt} + 0.311), \quad (A.7)$$

Here, c_{salt} denotes the electrolyte concentration, and ϵ represents the electrode porosity, which is set to 0.51 based on the value estimated in Ref. [15].

A.2 Gibbs sampling

To sample from the high-dimensional probability density function defined by the Kirchhoff MRF in Eq. (8), we employ a Gibbs sampling algorithm. Gibbs sampling is a type of Markov chain Monte Carlo (MCMC) method. At each update step, one variable

is selected from the high-dimensional state variables, a sample is drawn from the conditional distribution of that variable, and the current state is updated with the sampled value. Repeating this procedure enables sampling from high-dimensional probability density functions or distributions for which direct sampling is difficult.

As described above, the probability density function treated in this study is independent at each time t . Therefore, Gibbs sampling is performed independently for each time. By completing the square, the conditional probability density functions for each state variable I_i , J_i , V_i , and r_i can be derived as Eqs. (A.8)–(A.19):

$$P(I_i | \{I_{/i}\}, \{J_i\}, \{V_i\}, \{r_i\}, \{I_{\text{LCO},i}(t)\}, \{V_{\text{LCO},i}(t)\}) \propto \exp\left(-\kappa_{I_i} \left(I_i - \frac{\mu_{I_i}}{\kappa_{I_i}}\right)\right), \quad (\text{A.8})$$

$$\kappa_{I_i} = \beta + \delta + \eta \left[\frac{1}{BV'(V_i + V_{\text{LCO},i}(t))} \right]^2, \quad (\text{A.9})$$

$$\mu_{I_i} = \beta I_{\text{LCO},i}(t) + \delta(J_i - J_{i+1}) + \eta \frac{BV(V_i + V_{\text{LCO},i}(t))}{BV'(V_i + V_{\text{LCO},i}(t))^2}, \quad (\text{A.10})$$

$$P(J_i | \{I_i\}, \{J_{/i}\}, \{V_i\}, \{r_i\}, \{I_{\text{LCO},i}(t)\}, \{V_{\text{LCO},i}(t)\}) \propto \exp\left(-\kappa_{J_i} \left(J_i - \frac{\mu_{J_i}}{\kappa_{J_i}}\right)\right), \quad (\text{A.11})$$

$$\kappa_{J_i} = 2\delta + \gamma r_i^2, \quad (\text{A.12})$$

$$\mu_{J_i} = \delta(J_{i+1} + J_{i-1} - I_{i+1} + I_i) - \gamma r_i (V_{i+1} - V_i), \quad (\text{A.13})$$

$$P(V_i | \{I_i\}, \{J_i\}, \{V_{/i}\}, \{r_i\}, \{I_{\text{LCO},i}(t)\}, \{V_{\text{LCO},i}(t)\}) \propto \exp\left(-\kappa_{V_i} \left(V_i - \frac{\mu_{V_i}}{\kappa_{V_i}}\right)\right), \quad (\text{A.14})$$

$$\kappa_{V_i} = 2\gamma + \eta, \quad (\text{A.15})$$

$$\mu_{V_i} = \gamma(V_{i+1} + V_{i-1} + r_i J_i - r_{i-1} J_{i-1}) + \eta(BV^{-1}(I_i) - V_{\text{LCO},i}(t)), \quad (\text{A.16})$$

$$P(r_i | \{I_i\}, \{J_i\}, \{V_i\}, \{r_{/i}\}, \{I_{\text{LCO},i}(t)\}, \{V_{\text{LCO},i}(t)\}) \propto \exp\left(-\kappa_{r_i} \left(r_i - \frac{\mu_{r_i}}{\kappa_{r_i}}\right)\right), \quad (\text{A.17})$$

$$\kappa_{r_i} = \gamma J_i^2 + 2\phi + \psi, \quad (\text{A.18})$$

$$\mu_{r_i} = -\gamma J_i (V_{i+1} - V_i) + \phi(r_{i+1} + r_{i-1}) + \psi \bar{r}. \quad (\text{A.19})$$

Here, $\{X_{/i}\}$ denotes the set of variables X_k ($k = 1, \dots, i-1, i+1, \dots, N$) excluding the i -th variable X_i . As mentioned above, because Eq. (10) includes the Butler–Volmer (BV) function that describes the nonlinearity at the solid–liquid interface, the high-dimensional probability density function defined by Eq. (8) is not a multivariate normal distribution. Therefore, in deriving Eqs. (A.8)–(A.10), we perform a first-order perturbation expansion of the BV function and approximate the conditional distributions as normal distributions. In addition, sampling at both ends of the electrode

is performed based on the conditional probability density functions in which the boundary-condition relations in Eq. (6) are substituted.

Based on these conditional probability density functions, we construct the Gibbs sampling algorithm shown in Algorithm A.1 and estimate the marginal posterior probabilities.

Algorithm A.1 Gibbs sampling for Kirchhoff MRF

Set interval, burn_in, max_loop.

Initialize $\{I_i\}, \{J_i\}, \{V_i\}, \{r_i\}$.

for loop = 0 to max_loop do

 for i = 0 to data length do

 Sampling I_i^{new} from

$$P(I_i | \{I_i\}, \{J_i\}, \{V_i\}, \{r_i\}, \{I_{LCO,i}(t)\}, \{V_{LCO,i}(t)\} | \beta, \delta, \eta, \gamma, \varphi, \psi, \bar{r}).$$

 update $I_i^{new} \rightarrow I_i$.

 Sampling J_i^{new} from

$$P(J_i | \{I_i\}, \{J_i\}, \{V_i\}, \{r_i\}, \{I_{LCO,i}(t)\}, \{V_{LCO,i}(t)\} | \beta, \delta, \eta, \gamma, \varphi, \psi, \bar{r}).$$

 update $J_i^{new} \rightarrow J_i$.

 Sampling r_i^{new} from

$$P(r_i | \{I_i\}, \{J_i\}, \{V_i\}, \{r_i\}, \{I_{LCO,i}(t)\}, \{V_{LCO,i}(t)\} | \beta, \delta, \eta, \gamma, \varphi, \psi, \bar{r}).$$

 update $r_i^{new} \rightarrow r_i$.

 Sampling V_i^{new} from

$$P(V_i | \{I_i\}, \{J_i\}, \{V_i\}, \{r_i\}, \{I_{LCO,i}(t)\}, \{V_{LCO,i}(t)\} | \beta, \delta, \eta, \gamma, \varphi, \psi, \bar{r}).$$

 update $V_i^{new} \rightarrow V_i$.

 end for

 if loop % interval == 0 AND loop > burn_in then

 Save the values $\{I_i\}, \{J_i\}, \{V_i\}, \{r_i\}$ as samples.

 end if

end for

Calculate the expectation of the samples and output the values of

$\{I_i\}, \{J_i\}, \{V_i\}, \{r_i\}$.

A.3 Hyperparameter setting

Table A.1 lists the values of the regularization parameters introduced in Eq. (4) for the three-layer NN. For the regularization parameter A associated with current conservation and the regularization parameter C that constrains the admissible SOC range, we set sufficiently large values within a range that does not cause numerical divergence, because these constraints must be satisfied physically and violations

should not occur during training. This ensures that the estimated SOC is always constrained to satisfy current conservation and remain within a physically reasonable range.

In contrast, the regularization parameter B controlling the spatial continuity of SOC was optimized by trial and error while considering the trade-off between loss of local structures due to excessive smoothing and noise amplification due to insufficient regularization. Similarly, the number of hidden-layer units K was determined by trial and error so that the stability and reproducibility of the estimated spatiotemporal SOC map are ensured.

Table A.2 lists the hyperparameter values used in the Kirchhoff MRF of Eq. (7). The Kirchhoff MRF is a hierarchical Bayesian model as shown in Fig. 4(C), and in principle, it is possible to sample the hyperparameters simultaneously. However, at present, it is difficult to obtain numerically stable convergence when estimating the hyperparameters together with the latent variables. Therefore, in this study, the hyperparameters are fixed to predetermined values.

For δ , the hyperparameter corresponding to the term enforcing Kirchhoff's first law, we set a sufficiently large value relative to the likelihood term within a range that does not make the estimation process numerically unstable, because this physical law must be satisfied as a constraint. This suppresses substantial deviations of the estimated current distribution from the physical law.

In addition, for the hyperparameter ψ associated with the regularization term that constrains the liquid-phase ohmic resistivity $r_i(t)$ to fluctuate around the reference resistivity \bar{r} , which is determined from the initial electrolyte concentration, we set $\psi = 1/\bar{r}^2$ so that the magnitude of the fluctuations is suppressed to a level comparable to \bar{r} . Furthermore, for the hyperparameter ϕ corresponding to the regularization term that enforces spatial continuity of the liquid-phase resistivity, we set $\phi = 0.1\beta$, taking into account both the balance with the likelihood term associated with the observation error of the current and the difference in scale among the variables.

On the other hand, it was confirmed that the hyperparameter γ for the term including the ohmic voltage loss in Li-ion transport along the z -direction, as well as the hyperparameter η for the term corresponding to the Butler-Volmer equation

describing the solid–liquid interfacial reaction, exert pronounced effects on the scale and physical plausibility of the estimated liquid–phase conductivity and potential distributions. Therefore, in this study, for each of γ and η , we prepared ten candidate values in the ranges of 0.01–10 times β and 10^{-6} – 10^{-3} times β , respectively, and determined γ and η by performing a two–dimensional grid search on the γ – η plane.

Figure A.1 shows the results of the two–dimensional grid search on the γ – η plane conducted under the initial electrolyte concentration of 0.3 M.

Figure A.1(A) shows the γ – η dependence of the liquid–phase potential gradient near the electrode edge at the end of charging. Physically, the potential gradient from the electrode edge toward the interior is required to be positive; therefore, the region where the potential gradient is positive represents a valid parameter range. When γ is small, the potential gradient tends to become negative.

Figure A.1(B) shows the γ – η dependence of the maximum value of the estimated liquid–phase conductivity over all times and all spatial positions. As η increases, the estimated conductivity becomes excessively large, tending to exceed electrochemically realistic values (i.e., greater than 3.4 mS cm⁻²). Therefore, it is desirable to select a region that yields conductivity values within the range expected under the experimental conditions while remaining as large as possible.

Figure A.1(C) shows the γ – η dependence of the difference between the estimated liquid–phase conductivity at the electrode center and at the electrode edge at the beginning of charging. Under the low–concentration condition, it is physically consistent that the conductivity near the electrode edge is higher than that at the electrode center immediately after charging begins, and the region satisfying this condition serves as a selection criterion. When γ is large, this condition tends not to be satisfied.

The pair γ – η that simultaneously satisfies the following three conditions—(i) the potential gradient is positive, (ii) the maximum conductivity is within an electrochemically feasible range and sufficiently large, and (iii) at the beginning of charging, the conductivity at the electrode edge is higher than that at the electrode center—corresponds to the point indicated by the black circle in the figure. In this study, the values at this point were adopted as the hyperparameters.

For initial electrolyte concentrations of 1 M and 2 M, the estimated conductivity at the electrode edge tended to be consistently lower than that at the electrode center regardless of γ . In addition, the potential gradient was always positive regardless of γ , satisfying physical consistency. In contrast, the spatial variations in the estimated liquid-phase conductivity were strongly dependent on η : when η was set too large, the estimated conductivity exhibited temporally and spatially unstable oscillations, tending to produce physically implausible behavior. Based on these results, we confirmed that using the same hyperparameter setting selected under the 0.3 M condition yields stable and physically reasonable estimates for both 1 M and 2 M. Therefore, the same hyperparameters were employed for all initial electrolyte concentration conditions in this study.

Table A.1. Regularization parameters of the three-layer NN

Parameter	Value
A	30
B	30
C	30
K	2

Table A.2. Hyperparameters of the Kirchhoff MRF

Parameter	Value
β	10^6
δ	10β
γ	0.2β
η	$5 \times 10^{-5}\beta$
ϕ	0.1β
ψ	$1/\bar{r}^2$

References

- [1] Tarascon, J.-M.; Armand, M. Issues and challenges facing rechargeable lithium batteries. *Nature* **2001**, *414*, 359–367.

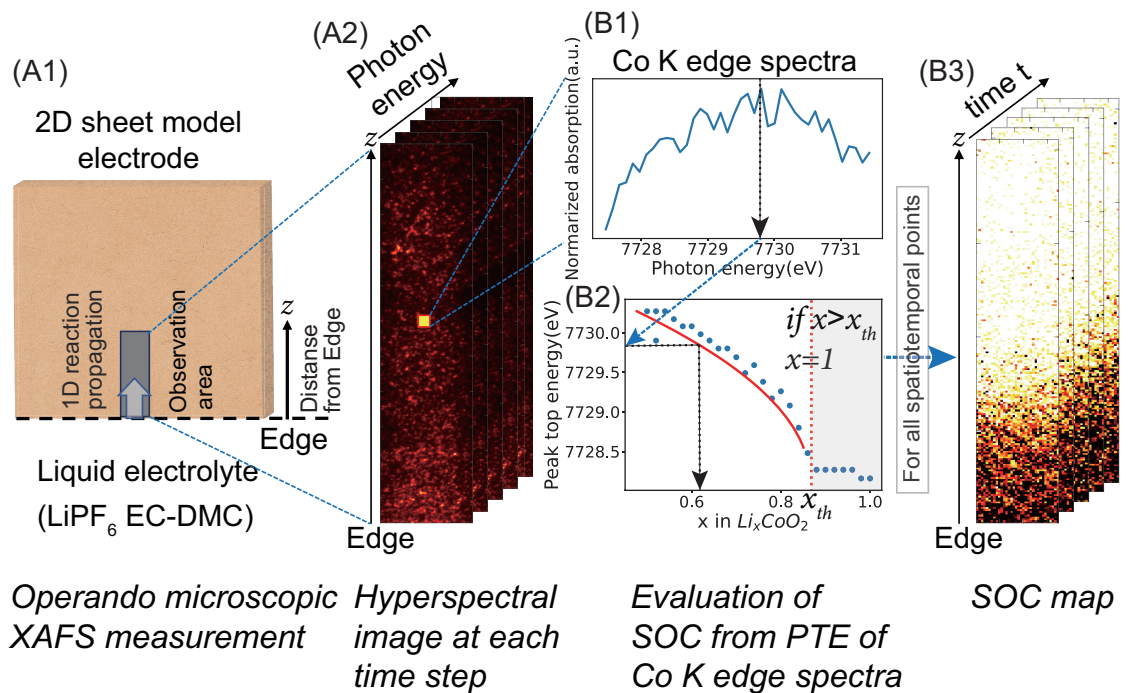
- [2] Simon, P.; Gogotsi, Y. Materials for electrochemical capacitors. *Nat. Mater.* **2008**, *7*, 845–854.
- [3] Dunn, B.; Kamath, H.; Tarascon, J.-M. Electrical energy storage for the grid: A battery of choices. *Science* **2011**, *334*, 928–935.
- [4] Nakamura, T.; Watanabe, T.; Kimura, Y.; Amezawa, K.; Nitta, K.; Tanida, H.; Ohara, K.; Uchimoto, Y.; Ogumi, Z. Visualization of inhomogeneous reaction distribution in the model LiCoO₂ composite electrode of lithium-ion batteries. *J. Phys. Chem. C* **2017**, *121*, 2118–2124.
- [5] Fergus, J. W. Recent developments in cathode materials for lithium-ion batteries. *J. Power Sources* **2010**, *195*, 939–954.
- [6] Etacheri, V.; Marom, R.; Elazari, R.; Salitra, G.; Aurbach, D. Challenges in the development of advanced Li-ion batteries: A review. *Energy Environ. Sci.* **2011**, *4*, 3243–3262.
- [7] Newman, J.; Thomas-Alyea, K. E. *Electrochemical Systems*, 3rd ed.; Wiley: Hoboken, NJ, 2004.
- [8] Liu, J.; Kunz, M.; Chen, K.; Tamura, N.; Richardson, T. J. Visualization of charge distribution in a lithium battery electrode. *J. Phys. Chem. Lett.* **2010**, *1*, 2120–2123.
- [9] Murayama, H.; Kitada, K.; Fukuda, K.; Mitsui, A.; Ohara, K.; Arai, H.; Uchimoto, Y.; Ogumi, Z.; Matsubara, E. Spectroscopic X-ray diffraction for microfocus inspection of Li-ion batteries. *J. Phys. Chem. C* **2014**, *118*, 20750–20755.
- [10] Strobridge, F. C.; Orvananos, B.; Croft, M.; Yu, H.-C.; Robert, R.; Liu, H.; Zhong, Z.; Connolly, T.; Drakopoulos, M.; Thornton, K.; et al. Mapping the inhomogeneous electrochemical reaction through porous LiFePO₄ electrodes in a standard coin cell battery. *Chem. Mater.* **2015**, *27*, 2374–2386.
- [11] Oriksa, Y.; Gogyo, Y.; Yamashige, H.; Katayama, M.; Chen, K.; Mori, T.; Yamamoto, K.; Masese, T.; Inada, Y.; Ohta, T.; et al. Ionic conduction in lithium-ion battery composite electrode governs cross-sectional reaction distribution. *Sci. Rep.* **2016**, *6*, 26382.

- [12] Chueh, W. C.; El Gabaly, F.; Sugar, J. D.; Bartelt, N. C.; McDaniel, A. H.; Fenton, K. R.; Zavadil, K. R.; Tyliszczak, T.; Lai, W.; McCarty, K. F. Intercalation pathway in many-particle LiFePO_4 electrode revealed by nanoscale state-of-charge mapping. *Nano Lett.* **2013**, *13*, 866–872.
- [13] Li, Y.; El Gabaly, F.; Ferguson, T. R.; Smith, R. B.; Bartelt, N. C.; Sugar, J. D.; Fenton, K. R.; Cogswell, D. A.; Kilcoyne, A. L. D.; Tyliszczak, T.; et al. Current-induced transition from particle-by-particle to concurrent intercalation in phase-separating battery electrodes. *Nat. Mater.* **2014**, *13*, 1149–1156.
- [14] Katayama, M.; Sumiwaka, K.; Miyahara, R.; Yamashige, H.; Arai, H.; Uchimoto, Y.; Ohta, T.; Inada, Y.; Ogumi, Z. X-ray absorption fine structure imaging of inhomogeneous electrode reaction in LiFePO_4 lithium-ion battery cathode. *J. Power Sources* **2014**, *269*, 994–999.
- [15] Nakamura, T.; Chiba, K.; Fakkao, M.; Kimura, Y.; Nitta, K.; Terada, Y.; Uchimoto, Y.; Amezawa, K. Operando observation of formation and annihilation of inhomogeneous reaction distribution in a composite electrode for lithium-ion batteries. *Batteries Supercaps* **2019**, *2*, 688–694.
- [16] Kimura, Y.; Tomura, A.; Fakkao, M.; Nakamura, T.; Ishiguro, N.; Sekizawa, O.; Nitta, K.; Uruga, T.; Okumura, T.; Tada, M.; et al. 3D operando imaging and quantification of inhomogeneous electrochemical reactions in composite battery electrodes. *J. Phys. Chem. Lett.* **2020**, *11*, 3629–3636.
- [17] Dawkins, J. I. G.; Ghavidel, M. Z.; Chhin, D.; Beaulieu, I.; Hossain, M. S.; Feng, R.; Mauzeroll, J.; Schougaard, S. B. Operando tracking of solution-phase concentration profiles in Li-ion battery positive electrodes using X-ray fluorescence. *Anal. Chem.* **2020**, *92*, 10908–10912.
- [18] Klamor, S.; Zick, K.; Oerther, T.; Schappacher, F. M.; Winter, M.; Brunklau, G. ^7Li in situ 1D NMR imaging of a lithium-ion battery. *Phys. Chem. Chem. Phys.* **2015**, *17*, 4458–4465.
- [19] Krachkovskiy, S. A.; Bazak, J. D.; Werhun, P.; Balcom, B. J.; Halalay, I. C.; Goward, G. R. Visualization of steady-state ionic concentration profiles formed in electrolytes during Li-ion battery operation and determination of mass-transport properties by in situ magnetic resonance imaging. *J. Am. Chem. Soc.* **2016**, *138*, 7992–7999.

- [20] Takamatsu, D.; Yoneyama, A.; Asari, Y.; Hirano, T. Quantitative visualization of salt concentration distributions in lithium-ion battery electrolytes during battery operation using X-ray phase imaging. *J. Am. Chem. Soc.* **2018**, *140*, 1608–1611.
- [21] Doyle, M.; Fuller, T. F.; Newman, J. Modeling of galvanostatic charge and discharge of the lithium/polymer/insertion cell. *J. Electrochem. Soc.* **1993**, *140*, 1526.
- [22] Doyle, M.; Newman, J. The use of mathematical modeling in the design of lithium/polymer battery systems. *Electrochim. Acta* **1995**, *40*, 2191–2196.
- [23] Yan, B.; Lim, C.; Yin, L.; Zhu, L. Three-dimensional simulation of galvanostatic discharge of LiCoO₂ cathode based on X-ray nano-CT images. *J. Electrochem. Soc.* **2012**, *159*, A1604.
- [24] Hutzenlaub, T.; Thiele, S.; Paust, N.; Spotnitz, R.; Zengerle, R.; Walchshofer, C. Three-dimensional electrochemical Li-ion battery modelling featuring a focused ion beam/scanning electron microscopy based three-phase reconstruction of a LiCoO₂ cathode. *Electrochim. Acta* **2014**, *115*, 131–139.
- [25] Ferraro, M. E.; Trembacki, B. L.; Brunini, V. E.; Noble, D. R.; Roberts, S. A. Electrode mesoscale as a collection of particles: Coupled electrochemical and mechanical analysis of NMC cathodes. *J. Electrochem. Soc.* **2020**, *167*, 013543.
- [26] Arora, P.; Doyle, M.; Gozdz, A. S.; White, R. E.; Newman, J. Comparison between computer simulations and experimental data for high-rate discharges of plastic lithium-ion batteries. *J. Power Sources* **2000**, *88*, 219–231.
- [27] Sulzer, V.; Marquis, S. G.; Timms, R.; Robinson, M.; Chapman, S. J. Python battery mathematical modelling (PyBaMM). *J. Open Res. Softw.* **2021**, *9*, 14.
- [28] Baliyan, A.; Imai, H. Machine learning-based analytical framework for automatic hyperspectral Raman analysis of lithium-ion battery electrodes. *Sci. Rep.* **2019**, *9*, 18241.
- [29] Nomura, Y.; Yamamoto, K.; Hirayama, T.; Ohkawa, M.; Igaki, E.; Hojo, N.; Saitoh, K. Quantitative operando visualization of electrochemical reactions and Li ions in all-solid-state batteries by STEM-EELS with hyperspectral image analyses. *Nano Lett.* **2018**, *18*, 5892–5898.

- [30] Nomura, Y.; Yamamoto, K.; Hirayama, T.; Igaki, E.; Saitoh, K. Visualization of lithium transfer resistance in secondary particle cathodes of bulk-type solid-state batteries. *ACS Energy Lett.* **2020**, *5*, 2098–2105.
- [31] Tanimoto, H.; Xu, H.; Mizumaki, M.; Seno, Y.; Uchiwada, J.; Yamagami, R.; Kumazoe, H.; Iwamitsu, K.; Kimura, Y.; Amezawa, K.; Akai, I.; Aonishi, T. Non-negative matrix factorization for 2D-XAS images of lithium-ion batteries. *J. Phys. Commun.* **2021**, *5*, 115005.
- [32] Hua, X.; Allan, P. K.; Geddes, H. S.; Castillo-Martinez, E.; Chater, P. A.; Dean, T. S.; Minelli, A.; Bruce, P. G.; Goodwin, A. L. Lithiation phase behaviors of metal oxide anodes and extra capacities. *Cell Rep. Phys. Sci.* **2021**, *2*, 100558.
- [33] Shiga, M.; Tatsumi, K.; Muto, S.; Tsuda, K.; Yamamoto, Y.; Mori, T.; Tanji, T. Sparse modeling of EELS and EDX spectral imaging data by non-negative matrix factorization. *Ultramicroscopy* **2016**, *170*, 43–59.
- [34] Nagata, K.; Sugita, S.; Okada, M. Bayesian spectral deconvolution with the exchange Monte Carlo method. *Neural Netw.* **2012**, *28*, 82–89.
- [35] Akai, I.; Iwamitsu, K.; Okada, M. Bayesian spectroscopy in solid-state photophysics. *J. Phys.: Conf. Ser.* **2018**, *1036*, 012022.
- [36] Iwamitsu, K.; Yokota, T.; Murata, K.; Kamezaki, M.; Mizumaki, M.; Uruga, T.; Akai, I. Spectral analysis of X-ray absorption near-edge structure in α -Fe₂O₃ based on Bayesian spectroscopy. *Phys. Status Solidi A* **2020**, *257*, 2000107.
- [37] Amatucci, G. G.; Tarascon, J.-M.; Klein, L. C. CoO₂, the end member of the Li_xCoO₂ solid solution. *J. Electrochem. Soc.* **1996**, *143*, 1114.
- [38] Ménétrier, M.; Saadoune, I.; Levasseur, S.; Delmas, C. The insulator-metal transition upon lithium deintercalation from LiCoO₂: Electronic properties and ⁷Li NMR study. *J. Mater. Chem.* **1999**, *9*, 1135–1140.
- [39] Bockris, J. O' M.; Reddy, A. K. N.; Gamboa-Aldeco, M. E. *Modern Electrochemistry 2A: Fundamentals of Electrodics*; Springer: New York, 2001.

- [40] Valøen, L. O.; Reimers, J. N. Transport properties of LiPF₆-based Li-ion battery electrolytes. *J. Electrochem. Soc.* **2005**, *152*, A882.
- [41] Nyman, A.; Behm, M.; Lindbergh, G. Electrochemical Characterisation and Modelling of the Mass Transport Phenomena in LiPF₆-EC-EMC Electrolyte. *Electrochim. Acta* **2008**, *53*, 6356–6365.
- [42] Garrido, L.; Mejía, A.; García, N.; Tiemblo, P.; Guzmán, J. Ion diffusion coefficients model and molar conductivities of ionic salts in aprotic solvents. *J. Phys. Chem. B* **2015**, *119*, 3097–3103.
- [43] Kingma, D. P.; Welling, M. Auto-encoding variational Bayes. *arXiv* **2013**, arXiv:1312.6114.
- [44] Lyu, Y.; Wu, X.; Wang, K.; Feng, Z.; Cheng, T.; Liu, Y.; Wang, M.; Chen, R.; Xu, L.; Zhou, J.; Lu, Y.; Guo, B. An Overview on the Advances of LiCoO₂ Cathodes for Lithium-Ion Batteries. *Adv. Energy Mater.* **2021**, *11*, 2000982.
- [45] Doyle, M.; Newman, J.; Gozdz, A. S.; Schmutz, C. N.; Tarascon, J.-M. Comparison of modeling predictions with experimental data from plastic lithium-ion cells. *J. Electrochem. Soc.* **1996**, *143*, 1890.
- [46] Ohzuku, T.; Ueda, A. Solid-state redox reactions of LiCoO₂ (R3m) for 4 V secondary lithium cells. *J. Electrochem. Soc.* **1994**, *141* (11), 2972–2977. <https://doi.org/10.1149/1.2059267>.



(C) Pipeline

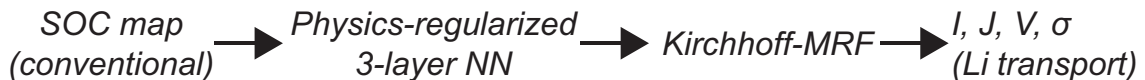


Figure 1. Hyperspectral data obtained by Co K-edge μ -XAFS measurements and the proposed analysis pipeline

(A) Schematic of operando micro-XAFS measurements for a two-dimensional sheet-type model electrode. (A1) Schematic illustration of the model electrode. The electrode edge is maintained at an equipotential, and the charge-discharge reaction proceeds one-dimensionally along the z -axis indicated in the figure. (A2) Example of a hyperspectral image acquired at a given time. Hyperspectral images are acquired at each time point during the progression of the charge-discharge reaction.

(B) Procedure for constructing an SOC map using the conventional method. (B1) Example of a Co K-edge XAFS spectrum at a given spatiotemporal point and the corresponding PTE. (B2) Relationship between PTE and SOC obtained from standard samples, together with a quadratic regression curve. For the PTE obtained at each spatiotemporal point, SOC is assigned based on the regression curve when $x < x_{th}$. In contrast, when $x > x_{th}$ (two-phase reaction region), SOC cannot be uniquely determined; therefore, the representative value of 1 is assigned. (B3) Example of SOC

maps at each time point obtained by the above procedure.

(C) Proposed analysis pipeline. For the SOC map obtained by the conventional method, a three-layer NN is regressed under physics-informed regularization to estimate SOC in the two-phase reaction region (see Fig. 2 for details). In addition, by using a Kirchhoff Markov random field (Kirchhoff MRF) based on a simplified porous-electrode model, internal states such as interfacial current, electrolyte current, potential, and conductivity in the Li-ion transport process are estimated (see Fig. 4 for details).

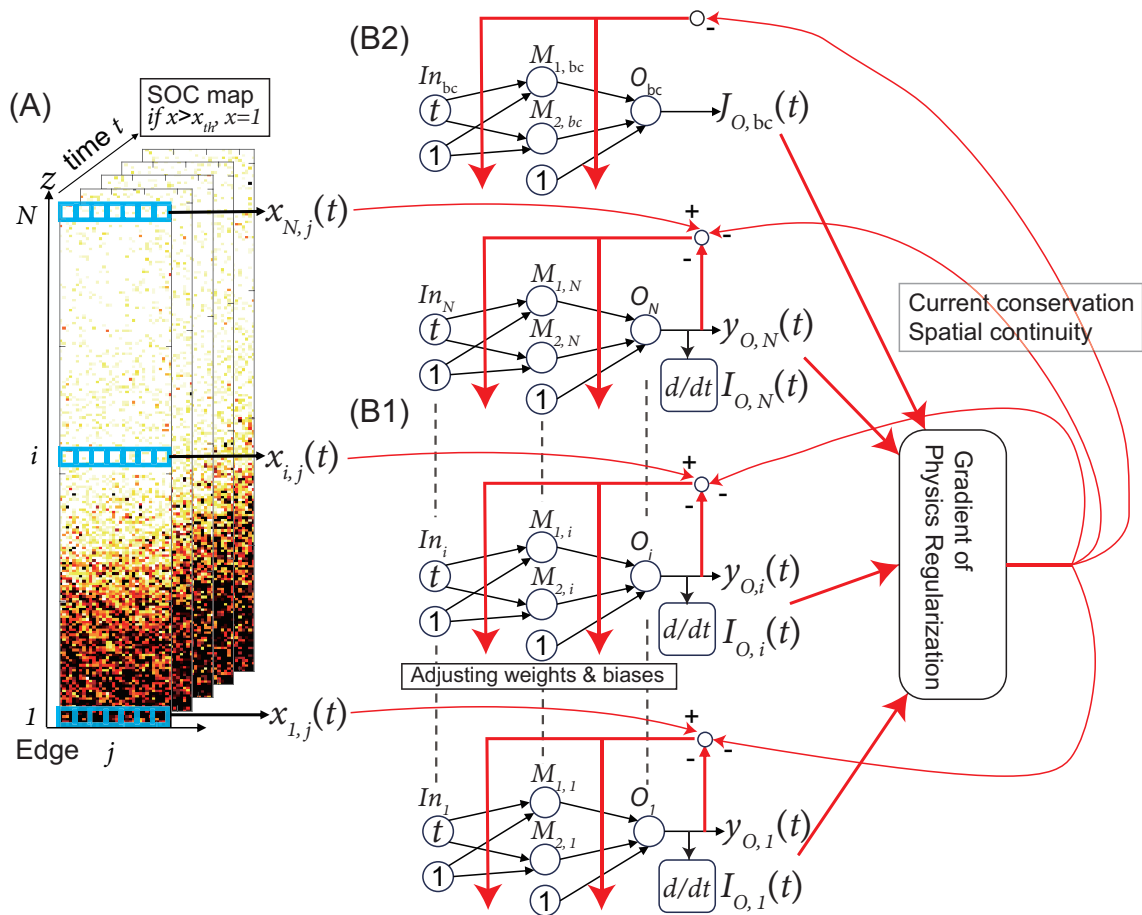


Figure 2. Data structure of the spatiotemporal SOC map and physics-regularized three-layer neural network

(A) Data structure of the spatiotemporal SOC map. The SOC at time t , pixel index i along the z -axis, and lateral pixel index j is defined as $x_{i,j}(t)$.

(B) Structure of the physics-regularized three-layer NN. (B1) For each pixel index i along the z direction ($i = 1, \dots, N$), the network consists of an input-layer cell In_i

that outputs time t , K hidden-layer cells $M_{1,i}$ to $M_{K,i}$ (in the figure, $K = 2$) with a sigmoid activation function, and an output-layer cell O_i with a linear activation function. Note that ① is a cell that outputs the constant 1, corresponding to the bias term. The output of O_i is $y_{O,i}(t)$, and its time derivative is interpreted as the current $I_{O,i}(t)$ corresponding to Li deintercalation/intercalation from/into LCO. **(B2)** Network representing the liquid-phase current at time t at $i = N + 1$, which is located outside the observation points in the z -direction, expressed using the same three-layer NN structure. Black lines indicate the forward signal flow of the network, and red lines indicate the signal flow during training. The connection weights are updated by considering not only the error between the SOC data $x_{i,k}(t)$ and the output $y_{O,i}(t)$, but also the gradients of the regularization terms based on SOC spatial continuity and current conservation.

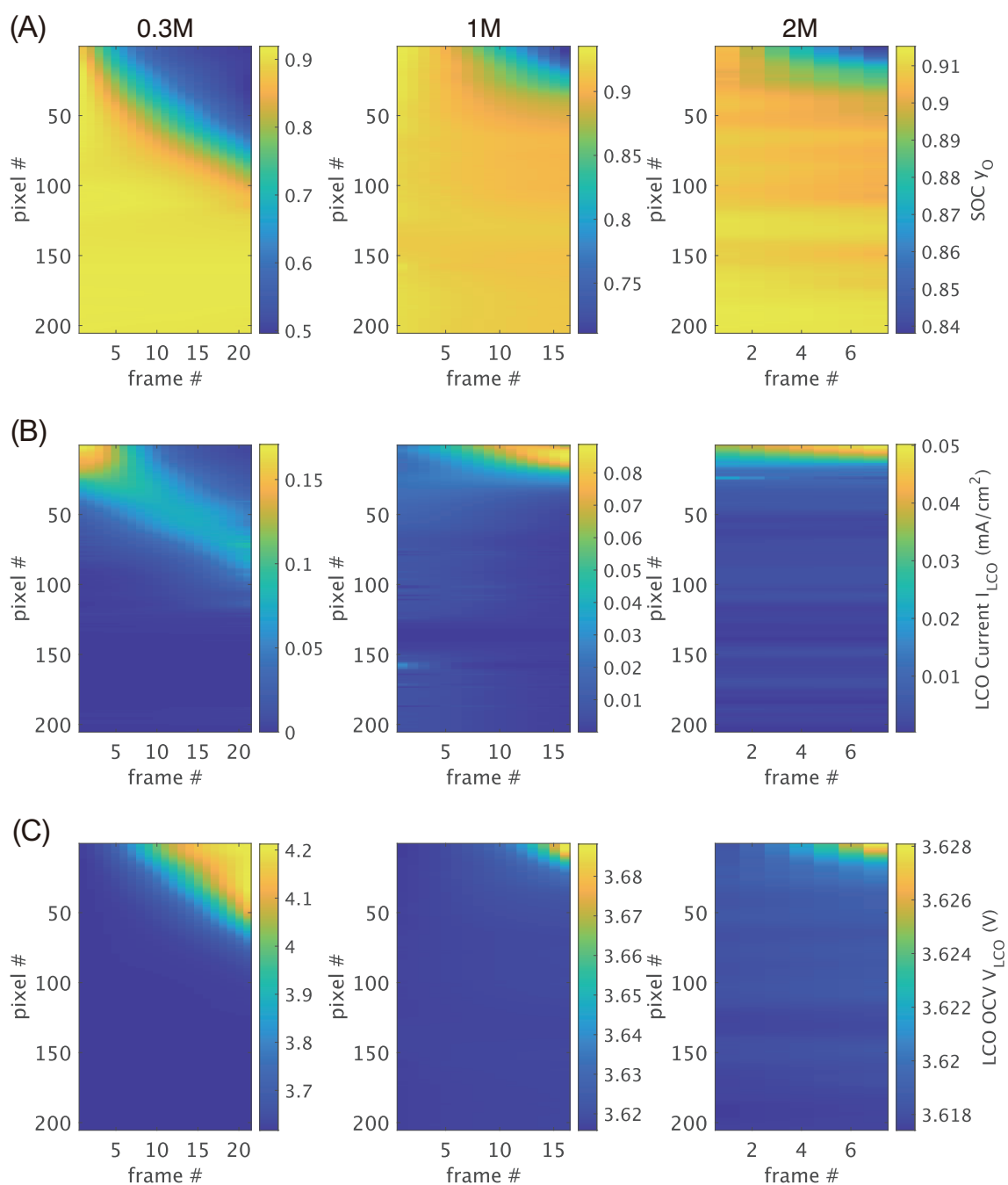


Figure 3. Estimated spatiotemporal SOC map including the two-phase reaction region, and estimated LCO current and open-circuit voltage

(A) Estimated spatiotemporal SOC maps including the two-phase reaction region, plotted from the trained NN output $y_{o,i}(t)$ for initial electrolyte concentrations of 0.3 M, 1 M, and 2 M.

(B) Spatiotemporal map of the LCO current. The current $I_{o,i}(t)$, obtained as the time derivative of the NN output $y_{o,i}(t)$ shown in (A), is assigned as the evaluated LCO current $I_{LCO,i}(t)$.

(C) Spatiotemporal map of the LCO OCV. By applying the LCO OCV curve (Eq. (A.1)) to the NN output $y_{o,i}(t)$ shown in (A), the LCO OCV $V_{LCO,i}(t)$ is calculated and plotted.

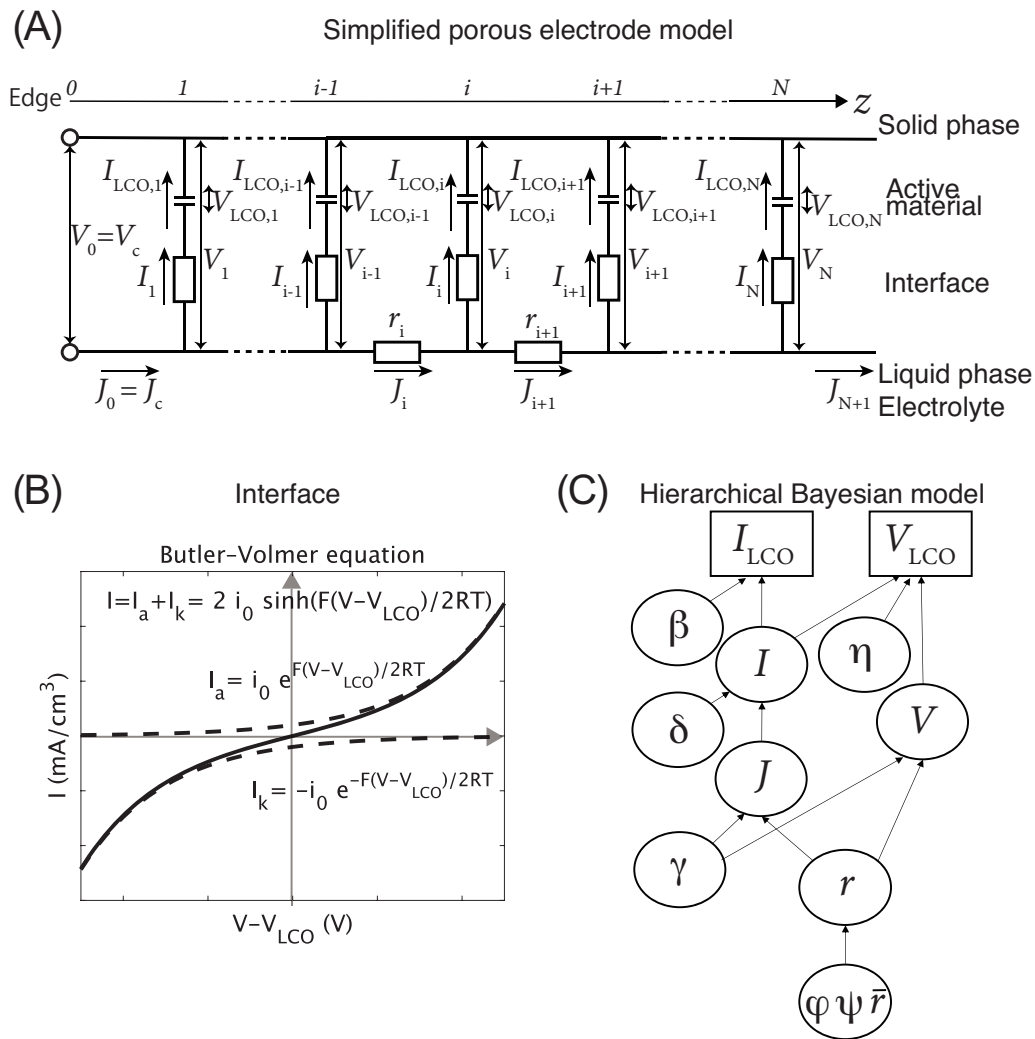


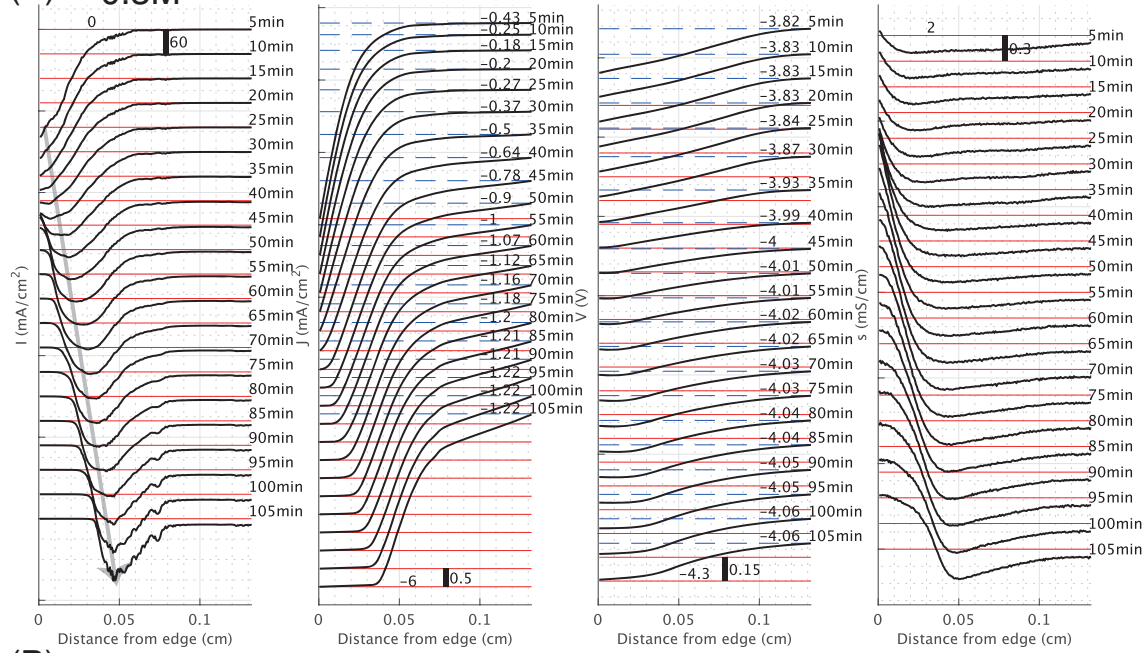
Figure 4. Kirchhoff Markov random field (Kirchhoff MRF) for estimating Li-ion transport processes

(A) Equivalent circuit based on a simplified porous-electrode model. Shown are the LCO current $I_{LCO,i}$, LCO OCV $V_{LCO,i}$, solid-liquid interfacial current I_i , liquid-phase current J_i , liquid-phase potential V_i , liquid-phase ohmic resistivity r_i , charging current J_c , charging voltage V_c , and the liquid-phase current J_{N+1} at $i = N + 1$ located outside the observation points along the z -direction.

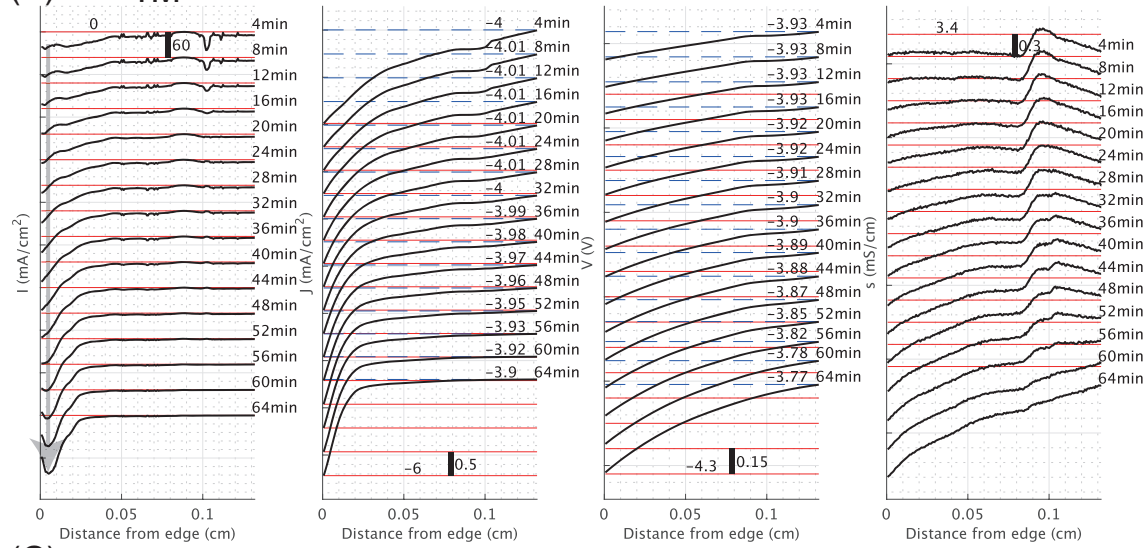
(B) Butler-Volmer (BV) equation governing the solid-liquid interfacial reaction. In this study, we use the expression limited to the case where the anodic and cathodic reactions are symmetric.

(C) Hierarchical Bayesian structure of the Kirchhoff MRF. The dependency relationships among state variables are represented based on equations derived from Kirchhoff's laws and Ohm's law in the equivalent circuit of the porous-electrode model.

(A) 0.3M



(B) 1M



(C) 2M

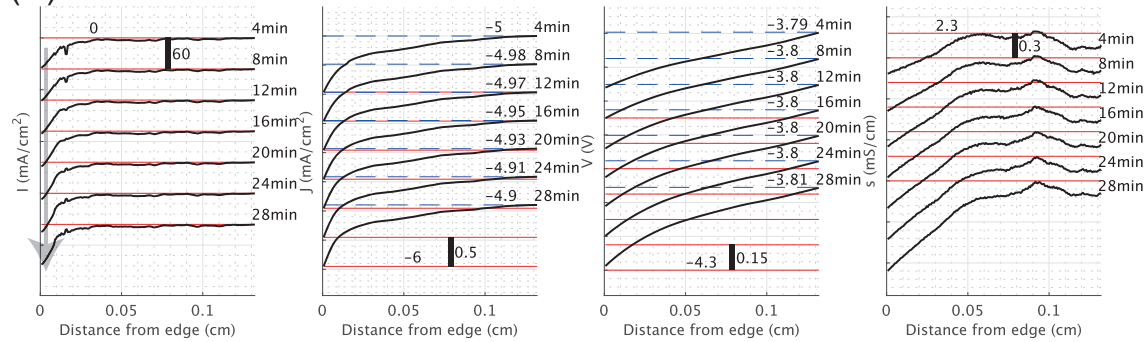


Figure 5. Analysis results of operando micro-spectroscopy data capturing the charging process using the proposed pipeline

Time evolution of the spatial distributions of the solid-liquid interfacial current I , liquid-phase current J , liquid-phase potential V , and liquid-phase ohmic conductivity s estimated by the proposed analysis pipeline. Results are shown for initial electrolyte concentrations of (A) 0.3 M, (B) 1 M, and (C) 2 M. Red lines indicate the reference value at each time point, and the numerical values are also shown. In the panels of J and V , light-blue dashed lines indicate the values of these states on the electrode-center side, and the numerical values are also shown.

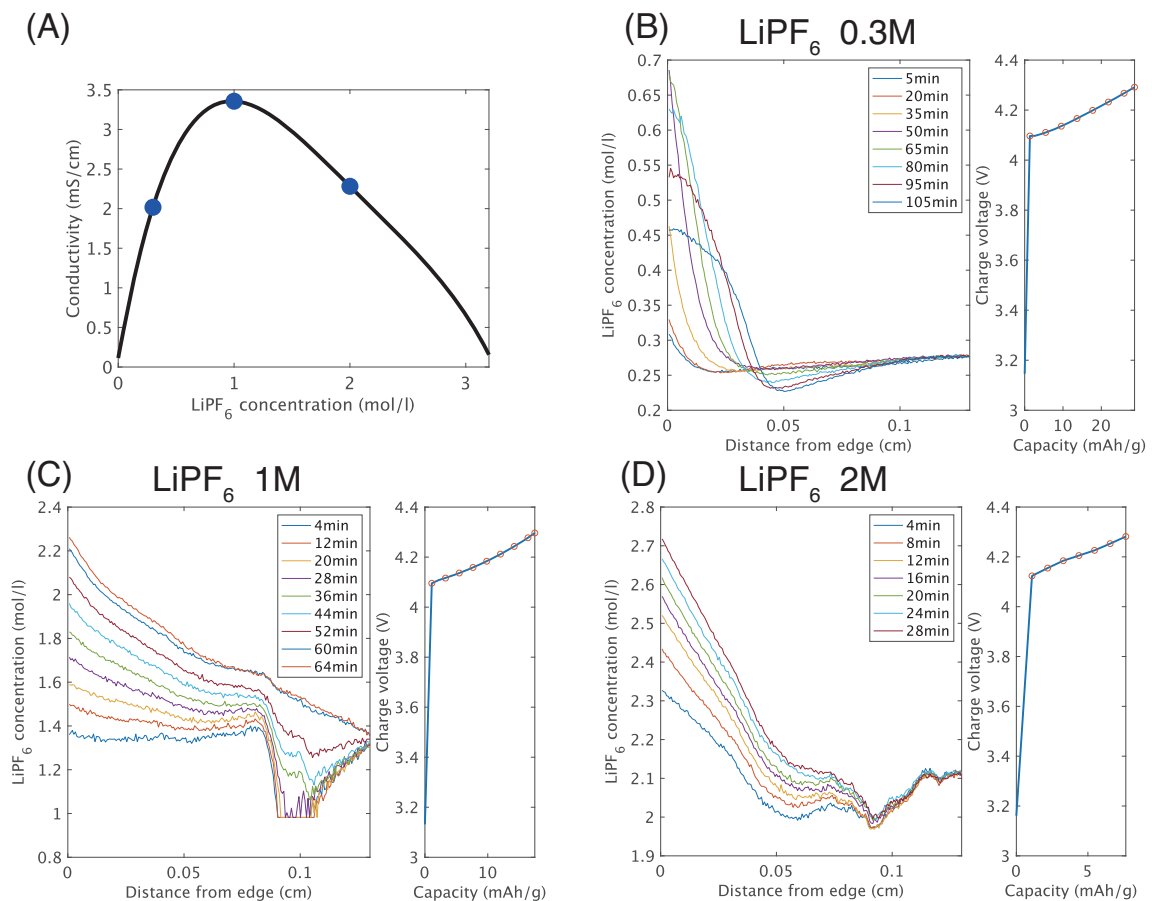


Figure 6. Prediction of electrolyte concentration based on the estimated conductivity

Results of predicting the electrolyte concentration from the estimated liquid-phase ohmic conductivity.

(A) Relationship between ionic conductivity and electrolyte concentration in an electrode device using LiPF_6 electrolyte, as expressed by Eq. (A.2). Blue circles indicate the conductivities under initial electrolyte concentrations of 0.3 M, 1 M, and 2 M.

The left panels in (B)–(D) show the time evolution of the spatial distribution of electrolyte concentration evaluated for sample electrode devices employing LiPF_6 , by applying the relationship in (A) to the estimated conductivity s in Fig. 4. The initial electrolyte concentrations are (B) 0.3 M, (C) 1 M, and (D) 2 M.

The right panels in (B)–(D) show the time evolution of the charging voltage and charge capacity for each electrode device.

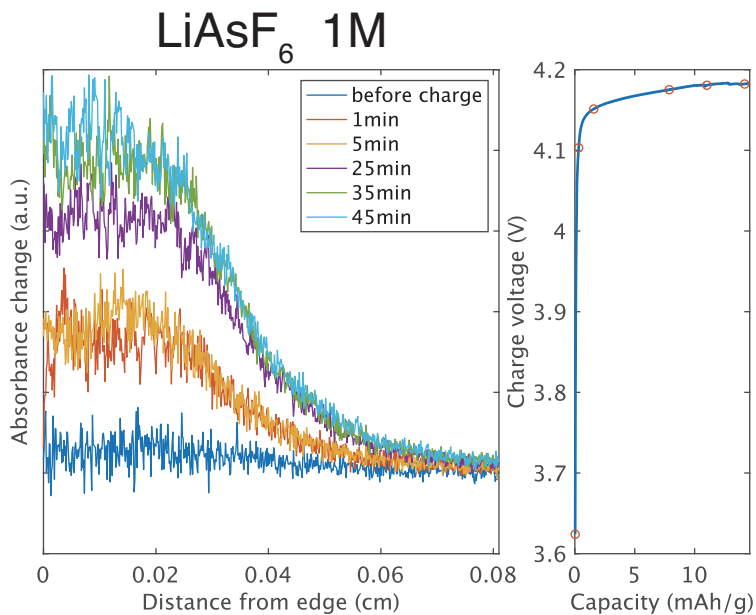


Figure 7. Direct operando measurement of electrolyte concentration distribution by X-ray transmission imaging

The left panel shows the time variation of the spatial distribution of electrolyte concentration in a sample electrode device employing LiAsF_6 as the electrolyte, obtained by operando measurements. The electrolyte concentration was evaluated from the difference in X-ray transmittance between transmission images acquired before and during charging. The right panels shows the time evolution of the charging voltage and charge capacity for this sample electrode device.

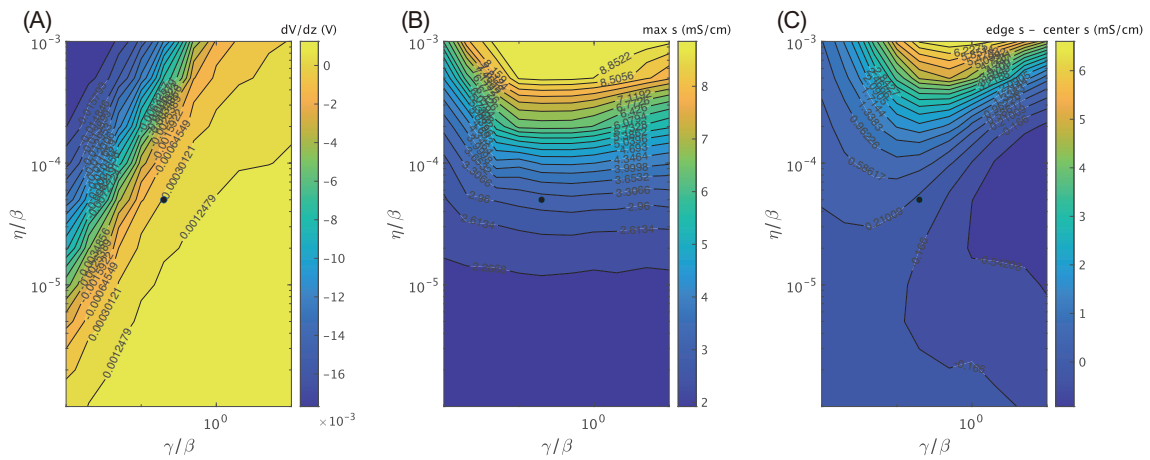


Figure A.1. Results of the two-dimensional grid search on the $\gamma - \eta$ plane

Dependence of the estimation results on γ and η under the initial electrolyte concentration condition of 0.3 M.

- (A) $\gamma - \eta$ dependence of the liquid-phase potential gradient near the electrode edge at the end of charging.
- (B) $\gamma - \eta$ dependence of the maximum value of the estimated liquid-phase conductivity over the entire spatiotemporal domain.
- (C) $\gamma - \eta$ dependence of the difference in the estimated liquid-phase conductivity between the electrode center and the electrode edge at the beginning of charging.

The black circle indicates the values of γ and η adopted in this study.